

# Oxidation Resistance and Microstructural Analysis of Polymer-Derived $(\text{Hf}_x\text{Ta}_{1-x})\text{C}/\text{SiC}$ Ceramic Nanocomposites

Nils-Christian Petry, Nathalie Thor, Jan Bernauer, Anke Silvia Ulrich, Emanuel Ionescu, Ralf Riedel, Astrid Pundt, Mathias Christian Galetz, and Maren Lepple\*

The oxidation behavior of polymer-derived  $(\text{Hf}_x\text{Ta}_{1-x})\text{C}/\text{SiC}$  nanocomposites at 1200 °C and 1400 °C for up to 100 h is investigated in this work. Overall, the chemical modification of the polycarbosilane-based precursor with Hf and Ta leads to an improved oxidation behavior due to an increased densification. Shifting the Hf/Ta ratio from  $(\text{Hf}_{0.2}\text{Ta}_{0.8})\text{C}/\text{SiC}$  to  $(\text{Hf}_{0.7}\text{Ta}_{0.3})\text{C}/\text{SiC}$  results in an improved oxidation behavior due to  $\text{Hf}_6\text{Ta}_2\text{O}_{17}$  formation and the reduction of  $\text{Ta}_2\text{O}_5$  formation, which reduces cracking of the samples. The formation and microstructure of  $\text{SiO}_2$  as well as the internal oxidation of  $(\text{Hf}_x\text{Ta}_{1-x})\text{C}$  precipitates is explained by thermodynamic and kinetic considerations.

To improve the oxidation resistance in this temperature range, a secondary silica-forming phase is typically added to the UHTC.<sup>[2,4,7,8]</sup>

Polymer-derived UHTC materials have received increased attention in the last few years due to their versatile processability. As the polymeric precursors are liquid or can be dissolved in organic solvents, they allow the usage of standard polymer deposition techniques namely dip, spray, or spin coating for the application as thermal (TBCs) or environmental barrier coatings (EBCs).<sup>[1,2,9,10]</sup> The synthesis technique of


using Si-based polymers modified with metal alkoxides or acetyl-acetonates as single-source precursors enables the production of polymer-derived ceramic nanocomposites (PDC-NCs) consisting of UHTC phases finely distributed in a silica-forming matrix such as SiC,  $\text{Si}_3\text{N}_4$  or SiCN.<sup>[1]</sup>

Recently, Wen et al.<sup>[6,8]</sup> prepared novel monolithic PDC-NCs with a microstructure consisting of nanosized  $(\text{Hf}_x\text{Ta}_{1-x})\text{C}$  solid-solution dispersed within a SiC matrix showing promising short-term high-temperature oxidation resistance. They investigated ceramic monoliths exposed to temperatures between 1200 °C and 1500 °C for up to 20 h and found an improved oxidation resistance compared to SiC/HfC through the incorporation of Ta. Wen et al. assumed that the oxides of the metal carbide

## 1. Introduction

Carbides, nitrides, and borides of group IV and V transition metals (such as  $\text{ZrB}_2$ , HfC, or TaC) are considered as ultra-high temperature ceramics (UHTCs).<sup>[1,2]</sup> They offer an attractive combination of properties such as ultra-high melting temperatures ( $\geq 3000$  °C), high chemical resistance, high hardness ( $\geq 20$  GPa), and Young's modulus ( $\geq 300$  GPa), making them an interesting class of materials for applications in extreme environments such as aero-propulsion, atmospheric re-entry, or hypersonic flight.<sup>[1,3–6]</sup> However, UHTCs provide poor oxidation resistance in the temperature range from 400 to 1600 °C due to the formation of a non-protective porous oxide scales such as  $\text{HfO}_2$  or  $\text{ZrO}_2$ .<sup>[4,7,8]</sup>

N.-C. Petry, A. S. Ulrich,<sup>[+]</sup> M. C. Galetz, M. Lepple<sup>[++]</sup>  
Materials and Corrosion  
DECHEMA-Forschungsinstitut  
Theodor-Heuss-Allee 25, D-60486 Frankfurt am Main, Germany  
E-mail: maren.lepple@anorg.chemie.uni-giessen.de

 The ORCID identification number(s) for the author(s) of this article can be found under <https://doi.org/10.1002/adem.202302023>.

<sup>[+]</sup>Present address: Metals and Alloys II, University of Bayreuth, Prof.-Rüdiger-Bormann-Straße 1, D-95447 Bayreuth, Germany

<sup>[++]</sup>Present address: Institute of Inorganic and Analytical Chemistry, Justus-Liebig-University Giessen, Heinrich-Buff-Ring 17, D-35392 Giessen, Germany

© 2024 The Authors. Advanced Engineering Materials published by Wiley-VCH GmbH. This is an open access article under the terms of the Creative Commons Attribution-NonCommercial License, which permits use, distribution and reproduction in any medium, provided the original work is properly cited and is not used for commercial purposes.

DOI: 10.1002/adem.202302023

N. Thor  
Institute of Applied Geosciences  
Technische Universität Darmstadt  
Schnittspahnstraße 9, D-64287 Darmstadt, Germany

J. Bernauer, E. Ionescu, R. Riedel  
Institut für Materialwissenschaft  
Technische Universität Darmstadt  
Otto-Berndt-Straße 3, D-64287 Darmstadt, Germany

E. Ionescu  
Fraunhofer Research Institution for Materials Recycling and Resource Strategies IWKS  
Brentanostraße 2a, D-63755 Alzenau, Germany

A. Pundt  
Institute for Applied Materials (IAM)  
Karlsruhe Institut für Technologie (KIT)  
Engelbert-Arnold-Straße 4, Karlsruhe D-76131, Germany

phases show an improved densification behavior leading together with the silica to the formation of a continuous protective oxide scale.<sup>[6,8]</sup>

However, detailed information on the microstructure of the formed oxide scale, oxidation mechanisms and kinetics as well as the long-term oxidation behavior of (Hf,Ta)C/SiC ceramic nanocomposites are still missing, which is the focus of this work. To elucidate the aforementioned points, monoliths of (Hf<sub>x</sub>Ta<sub>1-x</sub>)C/SiC ceramic nanocomposites were produced via the polymer-derived processing route and subsequent consolidation using field-assisted sintering technique (FAST). Two Si(Hf<sub>x</sub>Ta<sub>1-x</sub>)C single-source precursors were synthesized with different Hf/Ta ratios ( $x = 0.2$  and  $x = 0.7$ ). Additionally, polymer-derived SiC was used as reference material. The samples were oxidized at 1200 and 1400 °C in synthetic air and their oxidation behavior was analyzed by thermogravimetric analysis (TGA) for up to 100 h. A comprehensive study of the resulting microstructure of the oxidized samples was conducted using a combination of different analysis methods.

## 2. Results

### 2.1. Measurement of the Oxidation Kinetics

The results of the oxidation experiments obtained by TGA investigations are summarized in **Figure 1**. The specific mass change as a function of exposure time is plotted with (see Figure 1a,c) and without the preheating step showing the isothermal part of the measurement (see Figure 1b,d). All three materials SiC, (Hf<sub>0.7</sub>Ta<sub>0.3</sub>)C/SiC, and (Hf<sub>0.2</sub>Ta<sub>0.8</sub>)C/SiC exhibit a significant mass loss during preheating and in some cases also in the first minutes of the isothermal part of the measurements. At both temperatures, the specific mass loss listed in **Table 1** is highest for SiC. (Hf<sub>0.2</sub>Ta<sub>0.8</sub>)C/SiC shows the lowest mass loss during preheating. The mass loss of the material with an increased Hf/Ta ratio (Hf<sub>0.7</sub>Ta<sub>0.3</sub>)C/SiC lies between the other two materials. Figure 1a shows that the maximum mass loss of the chemically modified samples at 1200 °C is reached in the first minutes of the isothermal part of the measurement, while SiC shows its

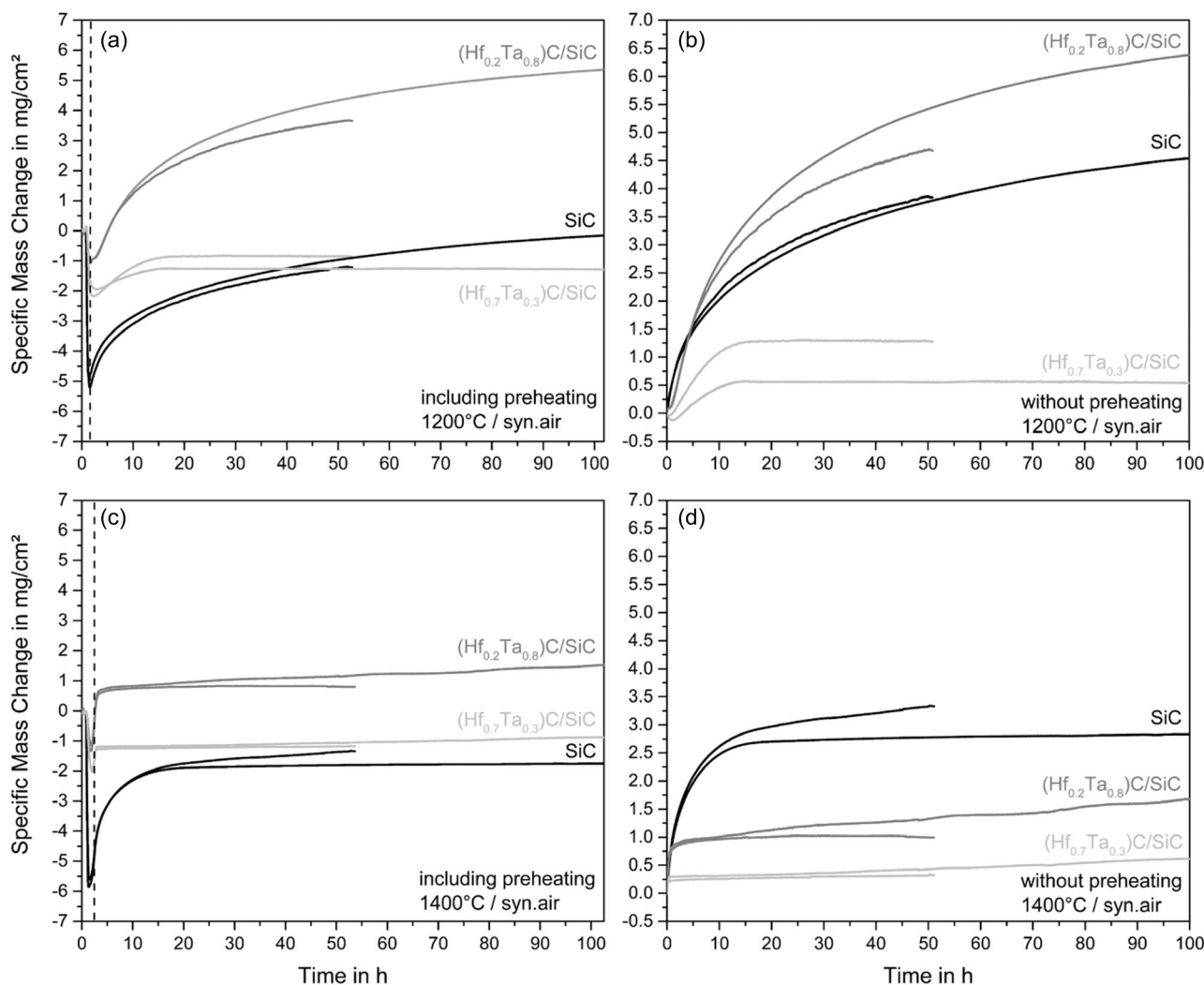


**Figure 1.** Specific mass change as a function of exposure time of (Hf<sub>x</sub>Ta<sub>1-x</sub>)C/SiC and SiC polymer-derived monoliths at 1200 °C a,b) and 1400 °C c,d) in synthetic air for 50 h and 100 h.

**Table 1.** Maximum specific mass loss during preheating and the mean specific (isothermal) mass gain after 50 and 100 h of  $(\text{Hf}_x\text{Ta}_{1-x})\text{C}/\text{SiC}$  and SiC polymer-derived monoliths after oxidation at 1200 and 1400 °C in synthetic air. Please note that for the 100 h values no uncertainty values are given, as just one sample of each material was measured for 100 h.

Temperature	SiC	$(\text{Hf}_{0.2}\text{Ta}_{0.8})\text{C}/\text{SiC}$	$(\text{Hf}_{0.7}\text{Ta}_{0.3})\text{C}/\text{SiC}$
Mean maximum specific mass loss during beginning of exposure in $\text{mg cm}^{-2}$			
1200 °C	$5.0 \pm 0.2$	$1.1 \pm 0.1$	$2.1 \pm 0.2$
1400 °C	$5.7 \pm 0.2$	$1.2 \pm 0.2$	$2.0 \pm 0.1$
Mean specific (isothermal) mass gain after 50 h in $\text{mg cm}^{-2}$			
1200 °C	$3.8 \pm 0.1$	$5.1 \pm 0.4$	$0.9 \pm 0.4$
1400 °C	$3.1 \pm 0.3$	$1.2 \pm 0.2$	$0.3 \pm 0.1$
Mean specific (isothermal) mass gain after 100 h in $\text{mg cm}^{-2}$			
1200 °C	4.5	6.4	0.5
1400 °C	2.8	1.7	0.6

maximum mass loss at the end of the preheating. The chemical modification with Hf and Ta leads to a decreased mass loss (up to 78% reduction) as compared to SiC.

The mean specific mass gain values after 50 and 100 h at 1200 and 1400 °C in synthetic air are also given in Table 1. The given data solely reflects the mass gain during the isothermal part. The initial mass loss during the preheating step is excluded. The uncertainties for the mean specific mass gain in Table 1 are calculated out of the two measurements per composition and isothermal temperature. Please note that for the 100 h values no uncertainty values are given, as just one sample of each material was measured for 100 h. The comparison of the three materials at 1200 °C shows that the material with the lower Hf/Ta ratio  $(\text{Hf}_{0.2}\text{Ta}_{0.8})\text{C}/\text{SiC}$  experienced the highest mass gain, while  $(\text{Hf}_{0.7}\text{Ta}_{0.3})\text{C}/\text{SiC}$  shows the lowest mass gain. The values for SiC are in between the chemically modified samples. This changes at 1400 °C, at this temperature SiC exhibits the highest mass gain. However, the total mass gain is lower compared to the 1200 °C samples (−18% after 50 h and −38% after 100 h).  $(\text{Hf}_{0.2}\text{Ta}_{0.8})\text{C}/\text{SiC}$  as well shows a significantly lower mass gain compared to the 1200 °C samples (−76% after 50 h and −73% after 100 h).

The overall comparison of the 1200 °C samples with the 1400 °C samples reveals lower mass gains for all three materials with increasing temperature from 1200 to 1400 °C.

The shape of the measured TGA curves differ significantly. At 1200 °C, SiC and  $(\text{Hf}_{0.2}\text{Ta}_{0.8})\text{C}/\text{SiC}$  show a strong mass increase in the first 10 h of isothermal oxidation and a subsequent parabolic-like shape with decreasing velocity of mass gain. Meanwhile,  $(\text{Hf}_{0.7}\text{Ta}_{0.3})\text{C}/\text{SiC}$  reflects a lower mass gain in the first 10 h at 1200 °C followed by rather a constant appearance with nearly no mass gain (see Figure 1b). At 1400 °C a significant change for SiC and  $(\text{Hf}_{0.2}\text{Ta}_{0.8})\text{C}/\text{SiC}$  is detected, as now all three materials show an initial fast increase in mass gain followed by a period with very low linear increase in mass gain. The initial mass gain in the first hours is lower compared to the 1200 °C samples, especially for  $(\text{Hf}_{0.2}\text{Ta}_{0.8})\text{C}/\text{SiC}$ . It takes less time (<5 h) until the plateau is reached.

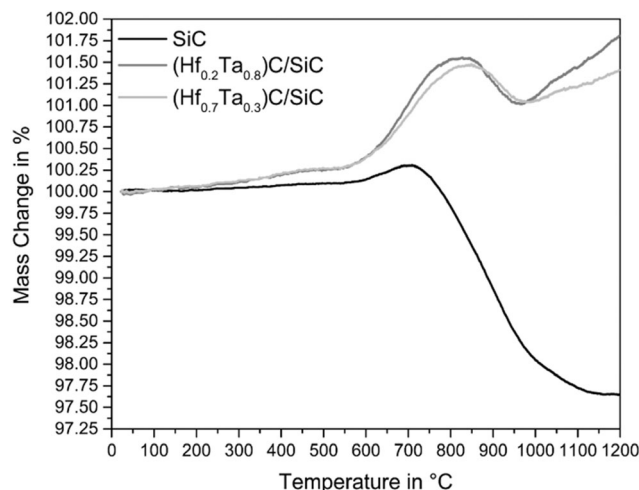


**Figure 2.** Via STA measured mass change with increasing temperature from room temperature to 1200 °C (heating rate:  $15\text{ °C min}^{-1}$ ) of  $(\text{Hf}_x\text{Ta}_{1-x})\text{C}/\text{SiC}$  and SiC polymer-derived monoliths in synthetic air.

Figure 2 represents the results of simultaneous thermal analysis (STA) measurements conducted to investigate the preheating step in more detail. The chemically modified samples show an initial slight increase in mass change (mass gain) starting at 200 °C, which significantly increases at  $\approx 600\text{ °C}$ . Starting at a temperature of 827 °C for  $(\text{Hf}_{0.2}\text{Ta}_{0.8})\text{C}/\text{SiC}$  and 848 °C for  $(\text{Hf}_{0.7}\text{Ta}_{0.3})\text{C}/\text{SiC}$  a relative negative mass change (mass loss) of in total 0.5 percentage points ( $(\text{Hf}_{0.2}\text{Ta}_{0.8})\text{C}/\text{SiC}$ ) and 0.4 percentage points ( $(\text{Hf}_{0.7}\text{Ta}_{0.3})\text{C}/\text{SiC}$ ) is detected. The relative mass loss ends when reaching 966 °C ( $(\text{Hf}_{0.2}\text{Ta}_{0.8})\text{C}/\text{SiC}$ ) and 989 °C ( $(\text{Hf}_{0.7}\text{Ta}_{0.3})\text{C}/\text{SiC}$ ), respectively. Afterwards again a mass gain is observed for both materials, whereas  $(\text{Hf}_{0.2}\text{Ta}_{0.8})\text{C}/\text{SiC}$  shows a stronger increase in mass gain compared to  $(\text{Hf}_{0.7}\text{Ta}_{0.3})\text{C}/\text{SiC}$ . The curve of SiC shows a mass gain in the temperature range between 600 and 700 °C, followed by a maximum relative mass loss of 2.7 percentage points in the temperature range between 711 and 1200 °C.

## 2.2. Characterization of Oxide Scales and Microstructural Evolution

A comprehensive investigation of the microstructure and mechanical properties of the sintered  $(\text{Hf}_{0.7}\text{Ta}_{0.3})\text{C}/\text{SiC}$  samples by using different electron microscopy techniques can be found in ref. [11]. As a summary, the microstructure of the samples after FAST-densification consists of finely distributed  $(\text{Hf}_x\text{Ta}_{1-x})\text{C}$  precipitates within the former powder particles, while a coarsening of the precipitates is detected at the boundaries of the former powder particles. Areas of pure  $\beta$ -SiC with larger grain sizes form between the former powder particles and are described as sinter necks. Nanosized pores (pore size up to  $\approx 30\text{ nm}$ ) are found within the former powder particles, while larger pores are found at the interface between former powder particles and the SiC sinter necks and within the SiC regions (pore size up to  $\approx 3\text{ }\mu\text{m}$ ). By evaluating scanning electron microscopy (SEM) images of cross-sections of the samples using an

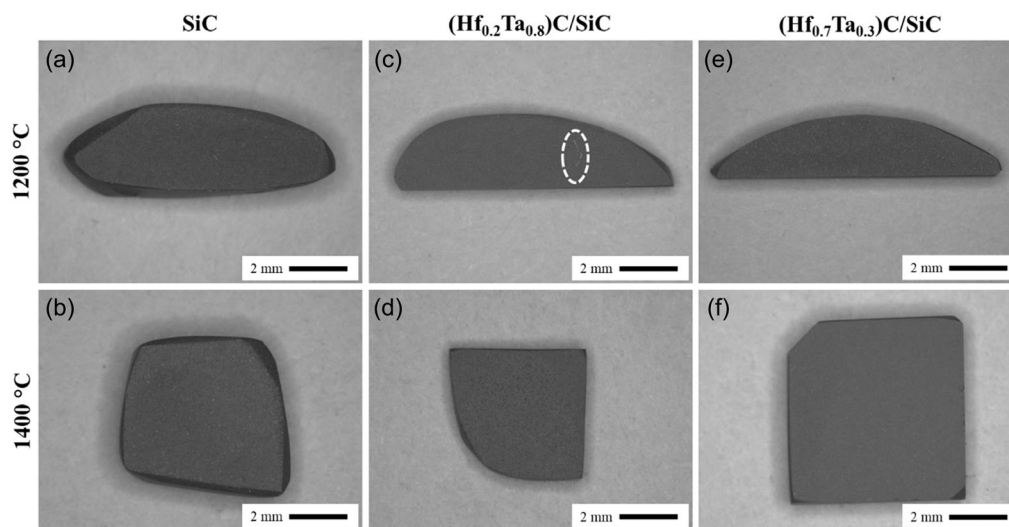


**Figure 3.** Macroscopic images of  $(\text{Hf}_x\text{Ta}_{1-x})\text{C}/\text{SiC}$  c–f) and SiC a,b) polymer-derived monoliths after 50 h of exposure at 1200 °C (a,c,e) and 1400 °C (b,d,f) in synthetic air.

image processing program<sup>[12]</sup> (ImageJ, National Institutes of Health, USA) a density of  $\approx 95\%$  was determined for the chemically modified samples  $(\text{Hf}_x\text{Ta}_{1-x})\text{C}/\text{SiC}$ ,<sup>[11]</sup> while the density of SiC is lower with  $\approx 91\%$  (this work).

**Figure 3** depicts macroscopic images of the samples after 50 h of exposure at 1200 and 1400 °C in synthetic air, respectively. The images show no voluminous oxides or massive cracking, indicating catastrophic oxidation. Solely, the image of the  $(\text{Hf}_{0.2}\text{Ta}_{0.8})\text{C}/\text{SiC}$  sample oxidized at 1200 °C displays one macroscopic crack (see marking Figure 3c). The tendency for  $(\text{Hf}_{0.2}\text{Ta}_{0.8})\text{C}/\text{SiC}$  showing crack formation during exposure is supported by experiments at 1400 °C and cross sections of the samples. In contrast, SiC and  $(\text{Hf}_{0.7}\text{Ta}_{0.3})\text{C}/\text{SiC}$  show a lower tendency to form cracks. Doubling the exposure time from 50 to 100 h does not significantly change the macroscopic appearance of the samples.

SEM surface investigations of each material after 50 h of exposure at 1200 °C in dry synthetic air show, that the decreased density and therefore increased porosity of SiC before exposure is found after oxidation as well (see **Figure 4**). While only isolated pores are found on the sample surface of the  $(\text{Hf}_x\text{Ta}_{1-x})\text{C}/\text{SiC}$  samples in the areas between the former powder particles, the sample surface of the oxidized SiC sample shows increased porosity with significantly larger pores. The measured porosities and pore sizes are summarized in **Table 2**. The porosities and pore sizes of the  $(\text{Hf}_x\text{Ta}_{1-x})\text{C}/\text{SiC}$  samples before oxidation were measured by Thor et al.<sup>[11]</sup> The measured porosity of the two chemically modified samples after oxidation is lower than the measured porosity before oxidation, while the porosity of the SiC sample before and after oxidation is unchanged. However, the porosity of SiC is significantly higher than that of the  $(\text{Hf}_x\text{Ta}_{1-x})\text{C}/\text{SiC}$  samples. The measured pore sizes are within the range of those within the cross sections of the samples before exposure (SiC: pore size up to  $\approx 20\ \mu\text{m}$  and  $(\text{Hf}_x\text{Ta}_{1-x})\text{C}/\text{SiC}$ : pore size up to  $\approx 3\ \mu\text{m}$ ). Nanosized porosity cannot be detected with the used magnifications of the SEM investigations.

The back scattered electron (BSE) images in **Figure 5** give an overview of the microstructure after 50 h of exposure in synthetic air at 1200 and 1400 °C, respectively. Electron probe micro analysis (EPMA) mapping was used to assess the degree of internal oxidation. The corresponding oxygen maps are included in **Figure 5**. All three materials show a high degree of internal oxidation at 1200 °C. The size of the depicted images displays approximately half of the cross-section thickness. Raising the temperature to 1400 °C leads to the formation of an internally oxidized zone in the chemically modified samples  $(\text{Hf}_x\text{Ta}_{1-x})\text{C}/\text{SiC}$  (see **Figure 5d,f**). The thickness of this layer is thinner for  $(\text{Hf}_{0.7}\text{Ta}_{0.3})\text{C}/\text{SiC}$  ( $210 \pm 9\ \mu\text{m}$ ) compared to that of  $(\text{Hf}_{0.2}\text{Ta}_{0.8})\text{C}/\text{SiC}$  ( $238 \pm 38\ \mu\text{m}$ ). Doubling the exposure time from 50 to 100 h leads to a slight increase in the thickness of the internally oxidized layer with  $248 \pm 11\ \mu\text{m}$  for  $(\text{Hf}_{0.7}\text{Ta}_{0.3})\text{C}/\text{SiC}$  and  $308 \pm 26\ \mu\text{m}$  for  $(\text{Hf}_{0.2}\text{Ta}_{0.8})\text{C}/\text{SiC}$ . The thickness was averaged over 10 individual element distribution measurements using the ImageJ software.<sup>[12]</sup> The mean value and the simple standard deviation are given. In contrast to the  $(\text{Hf}_x\text{Ta}_{1-x})\text{C}/\text{SiC}$  samples, SiC shows a high degree of internal oxidation at both temperatures.

The oxygen distribution maps in **Figure 5** show spots where the oxygen content is increased. EPMA maps (see **Figure S1**, Supporting Information) of the samples illustrate that these areas are found at the grain boundaries of the former SiC powder particle. In addition,  $(\text{Hf}_{0.2}\text{Ta}_{0.8})\text{C}/\text{SiC}$  experiences a higher degree of internal oxidation compared to that of  $(\text{Hf}_{0.7}\text{Ta}_{0.3})\text{C}/\text{SiC}$ .

BSE images with higher magnification were used to further investigate the microstructure close to the exposed samples surface (see **Figure 6**). Corresponding element maps were measured with energy-dispersive X-ray spectroscopy (EDS) (see **Figure S2–S4**, Supporting Information). At both temperatures SiC shows a thin oxide scale ( $\text{SiO}(\text{C})$ ) and a significant amount of porosity (see **Figure 6a,b**). The porosity stretches out over the whole bulk phase (see **Figure 5a,b**). Qualitative measurements using SEM/EDS reveal the formation of an



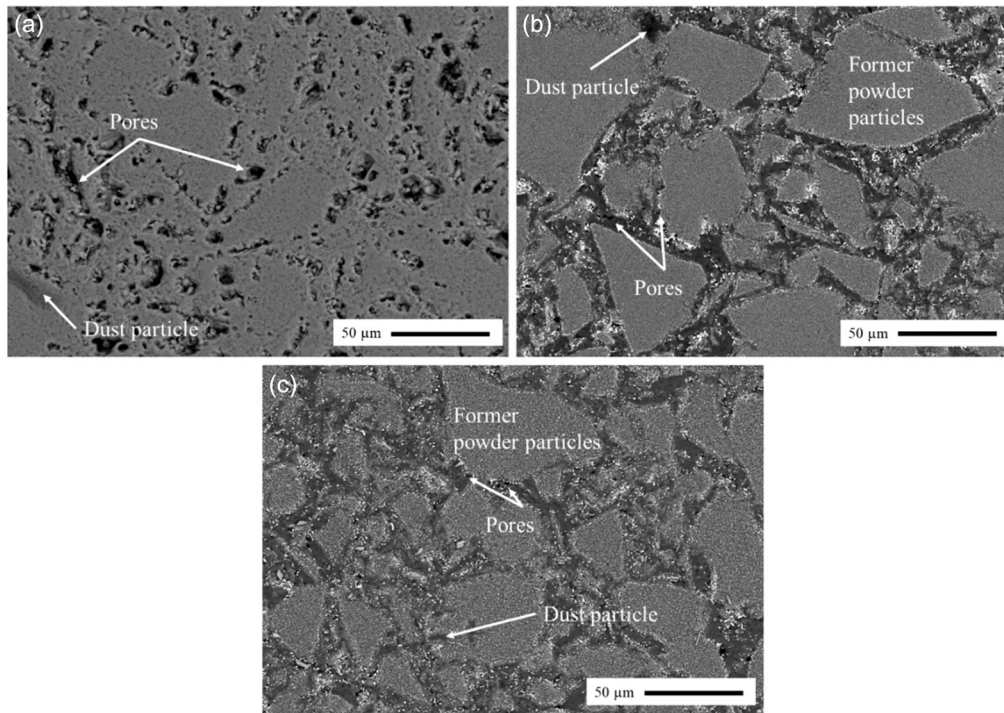


**Figure 4.** BSE images of the surface of the a) SiC, b)  $(\text{Hf}_{0.2}\text{Ta}_{0.8})\text{C}/\text{SiC}$ , and c)  $(\text{Hf}_{0.2}\text{Ta}_{0.8})\text{C}/\text{SiC}$  sample after 50 h of exposure at 1200 °C in dry synthetic air.

**Table 2.** Measured porosities and pore sizes of SiC and  $(\text{Hf}_x\text{Ta}_{1-x})\text{C}/\text{SiC}$  before<sup>[11]</sup> and after exposure at 1200 °C for 50 h in dry synthetic air.

Composition	SiC	$(\text{Hf}_{0.2}\text{Ta}_{0.8})\text{C}/\text{SiC}$	$(\text{Hf}_{0.7}\text{Ta}_{0.3})\text{C}/\text{SiC}$
Porosity before oxidation	9%	5% <sup>[11]</sup>	5% <sup>[11]</sup>
Pore size before oxidation	$\leq 20 \mu\text{m}$	$\leq 3 \mu\text{m}$ <sup>[11]</sup>	$\leq 3 \mu\text{m}$ <sup>[11]</sup>
Porosity after oxidation (50 h at 1200 °C)	9%	1.5%	1.5%
Pore size after oxidation (50 h at 1200 °C)	$\leq 20 \mu\text{m}$	$\leq 3 \mu\text{m}$	$\leq 3 \mu\text{m}$

oxygen-containing scale at the edges of the pores for SiC (see Figure S2, Supporting Information). The images of the  $(\text{Hf}_x\text{Ta}_{1-x})\text{C}/\text{SiC}$  samples and the corresponding SEM/EDS maps display a more complex microstructure (see Figure 6c–f, S3 and S4, Supporting Information). At both temperatures the samples show the formation of Hf- and Ta- containing oxides  $(\text{Hf,Ta})\text{O}$  in the intergranular areas between the former powder particles, which partially align to a line (whitish line in Figure 6e). In addition, SiC grains start to oxidize in the areas close to Hf- and Ta-containing oxides. Inside the former powder particles  $(\text{Hf}_x\text{Ta}_{1-x})\text{C}$  precipitates can be found. At the surface the samples develop a thin mainly Si-based oxide scale  $(\text{SiO}(\text{C}))$  with the incorporation of  $(\text{Hf,Ta})\text{O}$ . Besides the higher degree of internal oxidation no significant differences of the developed microstructure can be observed between the samples oxidized at 1200 °C and 1400 °C. The BSE images of the  $(\text{Hf}_{0.7}\text{Ta}_{0.3})\text{C}/\text{SiC}$  samples and the  $(\text{Hf}_{0.2}\text{Ta}_{0.8})\text{C}/\text{SiC}$  reveal no significant

differences, except the higher tendency to form cracks for  $(\text{Hf}_{0.2}\text{Ta}_{0.8})\text{C}/\text{SiC}$ .

The thickness of the outer oxide scale was determined based on the oxygen maps using the software ImageJ.<sup>[12]</sup> The mean oxide layer thicknesses from 10 individual measurements are listed in Table 3. The uncertainty is given as the simple standard deviation. Overall, the thickness of the oxide scale of the three materials does not differ significantly. After 50 h of exposure at 1200 °C the three materials form an oxide scale of  $\approx 0.5 \mu\text{m}$  thickness. The thickness increases with a higher oxidation temperature of 1400 °C to  $\approx 0.9 \mu\text{m}$ . Doubling the exposure time leads to a slight increase in oxide scale thickness. The measured scale thickness after 100 h of exposure lies in the range of  $\approx 0.6\text{--}0.9 \mu\text{m}$  at 1200 °C and  $\approx 0.9\text{--}1.2 \mu\text{m}$  at 1400 °C.

Closer investigations of the  $(\text{Hf}_x\text{Ta}_{1-x})\text{C}$  precipitates reveal a change in shape when oxidized. Figure 7 illustrates the change of the shape from spherical  $(\text{Hf}_x\text{Ta}_{1-x})\text{C}$  (white areas in Figure 7a–c) in the non-oxidized sample to irregular, ridged shapes, lined up in a chain, of the formed oxides (white areas in Figure 7d–f) in the oxidized sample. This change can be observed in both  $(\text{Hf}_x\text{Ta}_{1-x})\text{C}/\text{SiC}$  materials independent of temperature or exposure time changes. It seems that the size of the  $(\text{Hf}_{0.7}\text{Ta}_{0.3})\text{C}/\text{SiC}$  oxide precipitates is slightly larger compared to  $(\text{Hf}_{0.2}\text{Ta}_{0.8})\text{C}/\text{SiC}$ .

Figure 8 shows a transmission electron microscopy (TEM)-bright field (TEM-BF) image with selected area electron diffraction (SAED) patterns and local EDS point measurements of an area close to the surface of a  $(\text{Hf}_{0.7}\text{Ta}_{0.3})\text{C}/\text{SiC}$  sample oxidized at 1200 °C for 100 h. The area consists of the initial phases  $\beta$ -SiC and minor amounts of  $(\text{Hf}_{0.7}\text{Ta}_{0.3})\text{C}$  as well as  $\text{Hf}_6\text{Ta}_2\text{O}_{17}$ , which

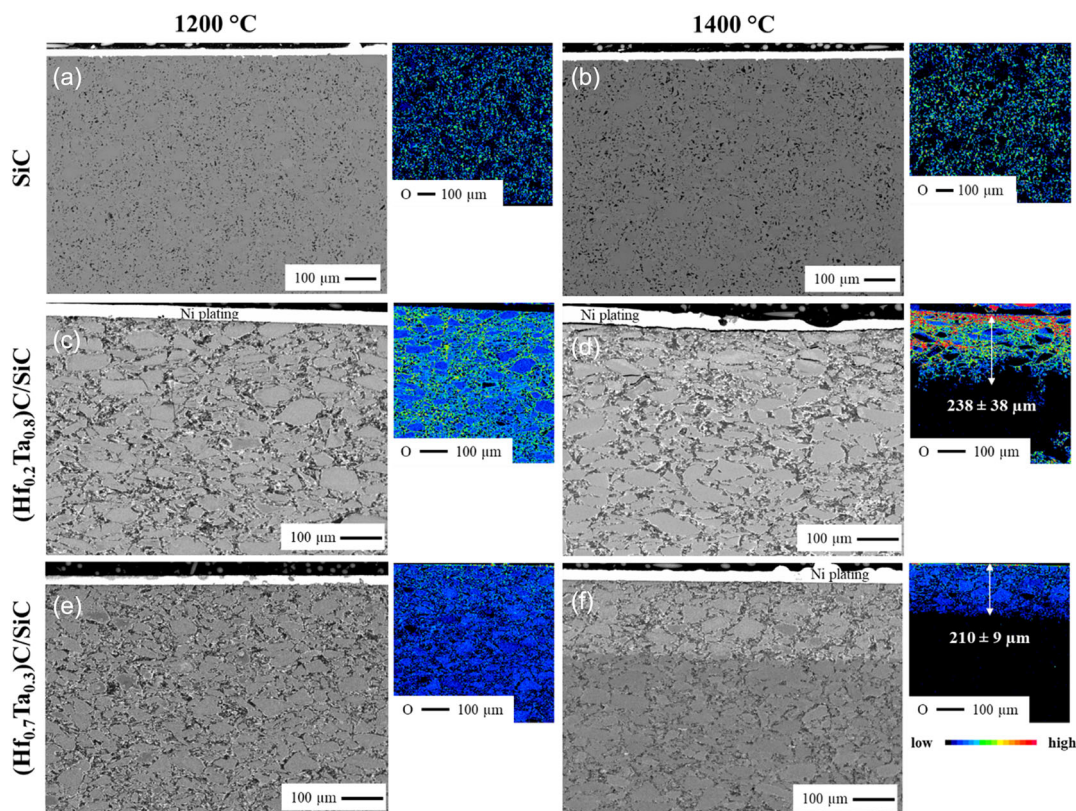


**Figure 5.** EPMA oxygen maps of cross sections of  $(\text{Hf}_x\text{Ta}_{1-x})\text{C}/\text{SiC}$  c–f) and SiC a,b) polymer-derived monoliths after exposure at 1200 °C (a,c,e) and 1400 °C (b,d,f) for 50 h in synthetic air.

can be confirmed via EDS measurements and SAED. The  $\beta$ -SiC shows a streaky appearance. The  $(\text{Hf}_{0.7}\text{Ta}_{0.3})\text{C}$  can be distinguished by its roundish form, whereas  $\text{Hf}_6\text{Ta}_2\text{O}_{17}$  shows cluster formation and an increase in size compared to the carbides.

**Figure 9** gives an overview of the phase composition at the surface of the samples before and after oxidation. Initially, the SiC sample consists of  $\alpha$ -SiC (PDF 72-0018) and  $\beta$ -SiC (PDF 74-2307). The modification of the used precursor with Hf and Ta-amido complexes led to the formation of  $(\text{Hf}_x\text{Ta}_{1-x})\text{C}$  phase ( $(\text{Hf}_{0.7}\text{Ta}_{0.3})\text{C}$ , PDF 19-6861). For the peaks of  $(\text{Hf}_x\text{Ta}_{1-x})\text{C}$  a shift towards higher  $2\theta$  values is detected with increasing Ta-content and consequently decreasing Hf/Ta ratios. Besides the  $(\text{Hf}_x\text{Ta}_{1-x})\text{C}$  phase, the phases of the initial precursor can be found. However, only  $\beta$ -SiC can be detected. All three materials show a peak at  $2\theta \approx 26.2^\circ$ , which can be attributed to free carbon in graphite form (PDF 75-1621). This peak disappears after oxidation. However, based on the X-ray diffraction (XRD) measurements no quantification of the content of the free carbon phase is possible. Despite the missing graphite signal, SiC experiences no significant change in phase composition after oxidation at 1200 °C for 50 h, whereas at 1400 °C the formation of crystalline  $\text{SiO}_2$  (cristobalite, PDF 39-1425) can be detected. The patterns of both  $(\text{Hf}_x\text{Ta}_{1-x})\text{C}/\text{SiC}$  materials show a  $\text{SiO}_2$  signal only at 1400 °C, whereas at 1200 °C characteristic peaks are missing. For the material with the lower Hf/Ta ratio,  $(\text{Hf}_{0.2}\text{Ta}_{0.8})\text{C}/\text{SiC}$  signals of orthorhombic  $\text{Ta}_2\text{O}_5$  (PDF 25-0922) and orthorhombic  $\text{Hf}_6\text{Ta}_2\text{O}_{17}$  (PDF 44-0998) can be detected at 1200 °C

(see Figure 9a). Besides the two oxides, phases of the sintered state are measured ( $\beta$ -SiC and  $(\text{Hf}_x\text{Ta}_{1-x})\text{C}$ ). The pattern of  $(\text{Hf}_{0.2}\text{Ta}_{0.8})\text{C}/\text{SiC}$  at 1400 °C shows the formation of the same oxides ( $\text{Ta}_2\text{O}_5$  and  $\text{Hf}_6\text{Ta}_2\text{O}_{17}$ ). The main difference compared to the 1200 °C pattern, despite the aforementioned  $\text{SiO}_2$  formation, is the detection of cubic TaC (PDF 35-0801) mainly attributed to the appearance of a peak at  $\approx 70^\circ$ .

The TaC formation at 1400 °C was also observed on the material with the higher Hf/Ta ratio  $(\text{Hf}_{0.7}\text{Ta}_{0.3})\text{C}/\text{SiC}$  (see Figure 9b). However, the patterns of  $(\text{Hf}_{0.7}\text{Ta}_{0.3})\text{C}/\text{SiC}$  show some significant differences to  $(\text{Hf}_{0.2}\text{Ta}_{0.8})\text{C}/\text{SiC}$  after oxidation. At both temperatures no  $\text{Ta}_2\text{O}_5$ -signal can be detected. Instead, the formation of monoclinic  $\text{HfO}_2$  (PDF 34-0104) and  $\text{Hf}_6\text{Ta}_2\text{O}_{17}$  can be observed at 1400 °C, whereas at 1200 °C only a  $\text{Hf}_6\text{Ta}_2\text{O}_{17}$  signal appears.

### 3. Discussion

#### 3.1. Oxidation Kinetics – Mass Loss

The TGA-curves (see Figure 1a,c) show a significant mass loss during preheating and the first hours of isothermal exposure of all three materials. This initial loss of mass is due to the formation of gaseous CO or  $\text{CO}_2$  by the oxidation of the free  $\text{sp}^2$ -hybridised carbon phase, which typically forms in-situ during pyrolysis of the polymeric precursor.<sup>[13]</sup> It has also been detected



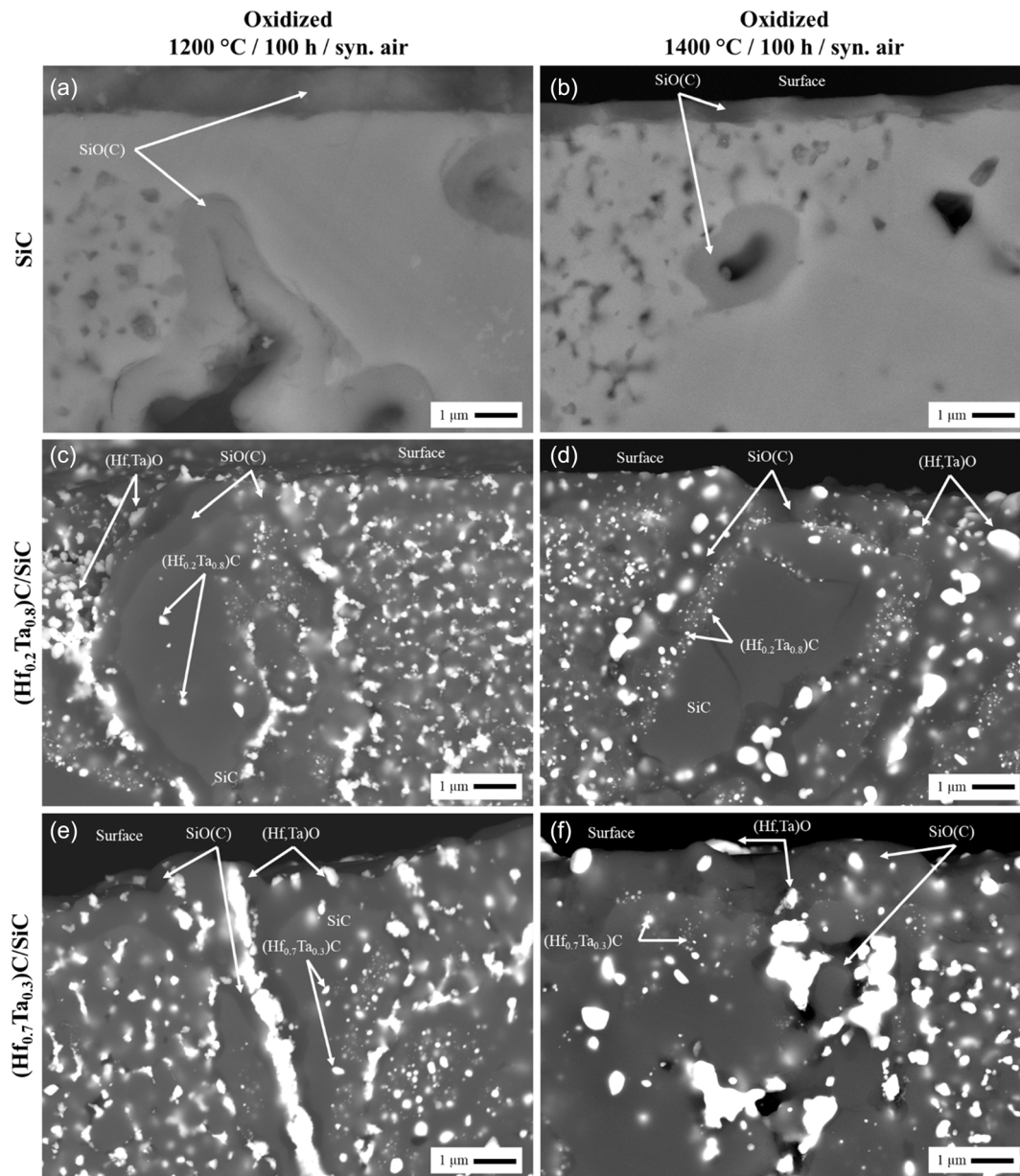


**Figure 6.** BSE images of cross sections of SiC a,b), (Hf<sub>0.2</sub>Ta<sub>0.8</sub>)C/SiC c,d) and (Hf<sub>0.7</sub>Ta<sub>0.3</sub>)C/SiC e,f) after exposure at 1200 °C (a,c,e) and 1400 °C (b,d,f) for 100 h in synthetic air.

**Table 3.** Mean thickness of the external oxide scale of (Hf<sub>x</sub>Ta<sub>1-x</sub>)C/SiC and SiC polymer-derived monoliths after exposure in synthetic air at 1200 and 1400 °C for 50 h and 100 h, respectively.

Temperature	SiC	(Hf <sub>0.2</sub> Ta <sub>0.8</sub> )C/SiC	(Hf <sub>0.7</sub> Ta <sub>0.3</sub> )C/SiC
Mean thickness of the external oxide scale after 50 h of exposure			
1200 °C	0.54 ± 0.1 μm	0.58 ± 0.2 μm	0.59 ± 0.2 μm
1400 °C	0.86 ± 0.1 μm	0.92 ± 0.2 μm	0.92 ± 0.1 μm
Mean thickness of the external oxide scale after 100 h of exposure			
1200 °C	0.58 ± 0.1 μm	0.69 ± 0.1 μm	0.87 ± 0.1 μm
1400 °C	1.09 ± 0.1 μm	0.93 ± 0.2 μm	1.23 ± 0.2 μm

by XRD (see Figure 9) and TEM characterization<sup>[11]</sup> of the samples before oxidation. STA-measurements were used to examine the preheating phase in more detail (see Figure 2). They indicate that most of the oxidation of the free carbon phase takes place in the temperature range between 700 and 1150 °C. However, the STA measurements also show that the samples experience a mass gain in addition to the mass loss during preheating. SiC experiences a significantly higher mass loss in the TGA as well as in the STA measurements compared to the two chemically modified samples (see Table 1), which is related to two factors.

First, the mass loss by the CO and CO<sub>2</sub> formation is superimposed by a mass gain due to the formation of solid oxide phases, which also impedes the exact determination of the share

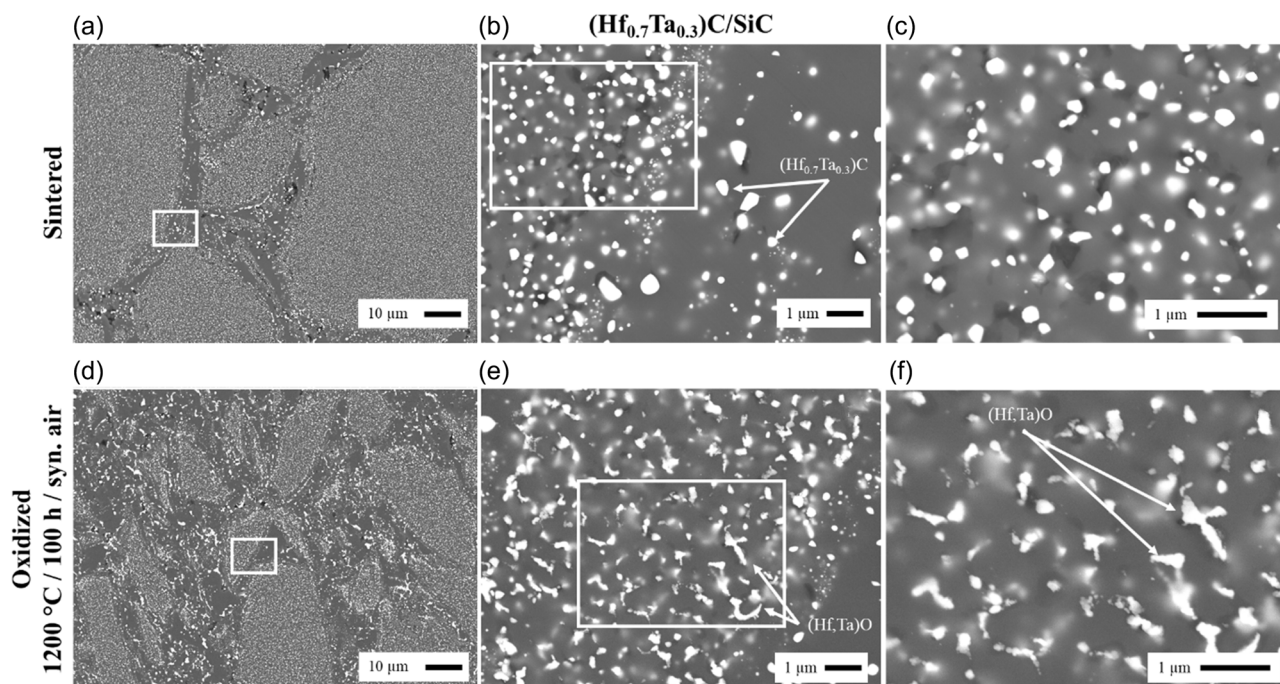


**Figure 7.** BSE images of  $(\text{Hf}_{0.7}\text{Ta}_{0.3})\text{C}/\text{SiC}$  in the sintered state a–c) and after exposure at 1200 °C for 100 h in dry synthetic air d–f).

of the C-oxidation on the total mass change. The assessment of the oxidation reactions of the respective carbides (SiC, HfC, and TaC) and therefore the formation of the solid oxide phases  $\text{SiO}_2$ ,  $\text{HfO}_2$ , and  $\text{Ta}_2\text{O}_5$  (see reactions 1, 2 and 4) shows, that all reactions lead to an increase in mass, despite the formation of gaseous CO and  $\text{CO}_2$ . While for the complete oxidation of HfC and SiC two oxygen atoms are added per Hf- and Si-atom, the complete oxidation of TaC leads to an addition of 2.5 oxygen atoms per Ta-atom. The oxidation of the free carbon phase, in contrast, results in a mass loss of one C-atom per CO or  $\text{CO}_2$  molecule formed. As the STA investigation shows, the oxidation of the transition metal carbides starts at lower temperatures as the oxidation of SiC, which is sluggish (see Section 4.4 below). In literature, the oxidation behavior of HfC and TaC as well as of solid solutions with different ratios of the two carbides show oxidation of TaC and HfC starting at 750 and 800 °C, respectively, whereas mixed carbides exhibited a higher oxidation onset temperature (80 vol% TaC-20 vol% HfC: 850 °C and 20 vol% TaC-80 vol% HfC: 900 °C).<sup>[14]</sup> The local maximum of the mass change of the  $(\text{Hf}_x\text{Ta}_{1-x})\text{C}/\text{SiC}$  samples in this work lies in the range of these values with 827 °C for  $(\text{Hf}_{0.2}\text{Ta}_{0.8})\text{C}/\text{SiC}$  and 848 °C for  $(\text{Hf}_{0.7}\text{Ta}_{0.3})\text{C}/\text{SiC}$  (see Figure 2). However, the samples already show a significant mass increase starting at a temperature of  $\approx 600$  °C. It must be considered that Zhang et al.<sup>[14]</sup> investigated monolithic samples of the mixed carbides without the SiC phase, which limits the comparability. Moreover, other studies detected oxidation reactions of HfC starting already at 40 °C<sup>[15]</sup> and 550 °C.<sup>[16]</sup> In addition, the  $(\text{Hf}_x\text{Ta}_{1-x})\text{C}$  are nanosized precipitates whose reactivity is higher than that of monolithic samples due to the high ratio of particle surface area to particle volume. Furthermore, the oxidation of the  $(\text{Hf}_x\text{Ta}_{1-x})\text{C}$  phase is strongly

thermodynamically favored, which is discussed in more detail in Section 4.4.

As a result, the inward diffusing oxygen is initially gettered by the oxidation of the  $(\text{Hf}_x\text{Ta}_{1-x})\text{C}$  precipitates and thus oxidation of the inner free carbon phase only takes place after the oxidation of the  $(\text{Hf}_x\text{Ta}_{1-x})\text{C}$  precipitates explaining the early mass gain before mass loss can be detected.

The lower porosity of the samples represents the second factor for the overall lower mass loss of the  $(\text{Hf}_x\text{Ta}_{1-x})\text{C}/\text{SiC}$  samples compared to SiC. Examination of the microstructure of the sintered SiC samples shows that they have an increased porosity of  $\approx 9\%$  (compared to  $\approx 5\%$  of the chemically modified samples) even before oxidation (see Table 2). After oxidation, a reduced porosity can be observed in the  $(\text{Hf}_x\text{Ta}_{1-x})\text{C}/\text{SiC}$  samples ( $\approx 1.5\%$ ), while the porosity of SiC does not change significantly, which is discussed in more detail in Section 4.3. The BSE image of the SiC sample surface after oxidation (see Figure 4a) shows that this is an open porosity. This results in facilitated inward diffusion of oxygen into the base material, which explains both the formation of a  $\text{SiO}(\text{C})$  phase around the pores as shown in Figure 6 and the significant internal oxidation of the SiC samples and, therefore, higher C-oxidation at both temperatures (see Figure 5a,b). The comparison of the porosity values also shows that the modification of the polymeric precursor with Hf and Ta improves the densification at given sintering parameters.

In addition to the comparison of the chemically modified samples with SiC, the behavior of the two  $(\text{Hf}_x\text{Ta}_{1-x})\text{C}/\text{SiC}$  samples in the preheating phase can also be compared to investigate the influence of the Hf/Ta ratio. It can be seen that  $(\text{Hf}_{0.2}\text{Ta}_{0.8})\text{C}/\text{SiC}$  shows a lower initial mass loss compared to  $(\text{Hf}_{0.7}\text{Ta}_{0.3})\text{C}/\text{SiC}$  (see Figure 1) and a more substantial increase directly following



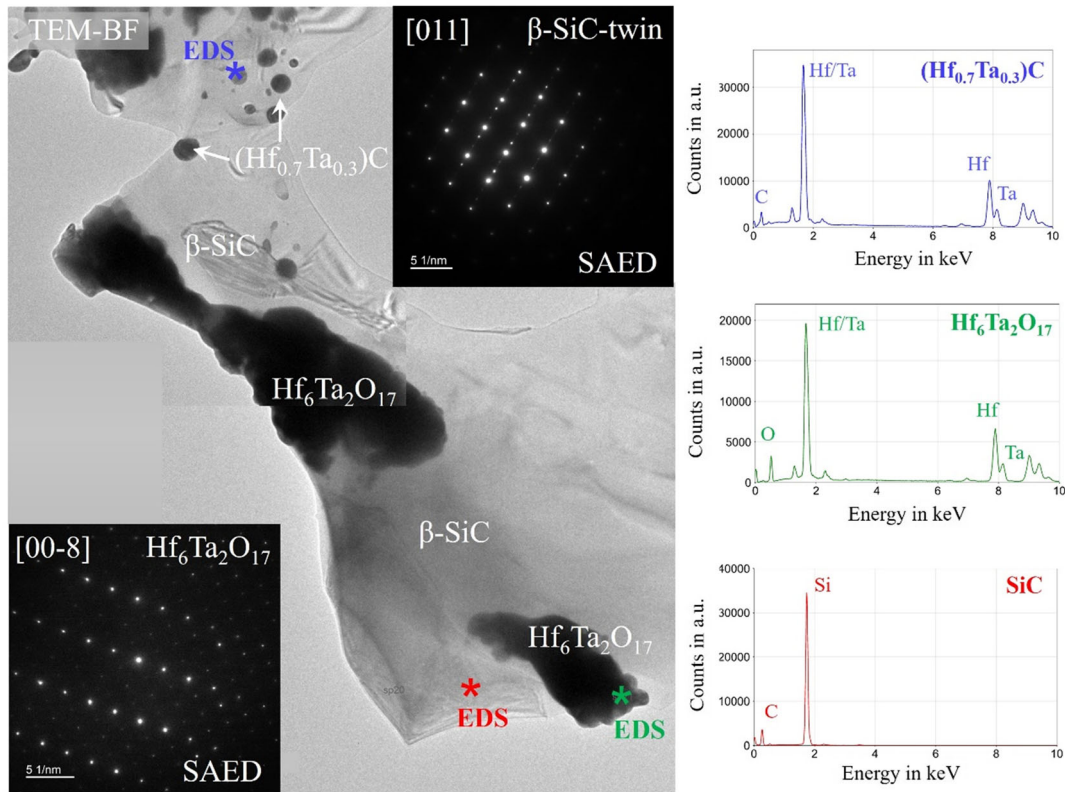


**Figure 8.** TEM bright-field image with SAED patterns and local EDS point measurements of an area close to the surface of a  $(\text{Hf}_{0.7}\text{Ta}_{0.3})\text{C}/\text{SiC}$  sample oxidized at  $1200\text{ }^{\circ}\text{C}$  in synthetic air for 100 h.

the mass loss (see Figure 2). The increased mass gain due to the oxidation of  $\text{TaC}$  ( $28\text{ g mol}^{-1}$ ) to  $\text{Ta}_2\text{O}_5$  compared to  $\text{SiC}$  and  $\text{HfC}$  ( $20\text{ g mol}^{-1}$ ) is a possible explanation for this behavior. Due to the higher Ta content (lower Hf/Ta ratio) of the samples, more  $\text{Ta}_2\text{O}_5$  is formed, as evidenced by the comparison of the measured X-ray diffractograms of the oxidized samples (see Figure 9a,b) and discussed in detail in the following Section 4.2. This results in a lower initial mass loss since the higher mass increase through the  $\text{Ta}_2\text{O}_5$  formation compensates more strongly the oxidation of the free carbon phase than the  $\text{HfO}_2$  formation. Additionally, a stronger mass increase also occurs afterwards. Prerequisite for this is that  $(\text{Hf}_{0.2}\text{Ta}_{0.8})\text{C}/\text{SiC}$  and  $(\text{Hf}_{0.7}\text{Ta}_{0.3})\text{C}/\text{SiC}$  show a comparable degree of oxidation attack during preheating, which, due to the very small differences in the microstructure of the samples (see Figure 6) and the similar curve progression (see Figure 2), can be assumed.

### 3.2. Oxidation Kinetics – Mass Gain

Following the initial mass loss, the TGA curves have a constant appearance with minor mass change, especially at  $1400\text{ }^{\circ}\text{C}$  (see Figure 1). The observed constant appearance is related to the formation of a protective  $\text{SiO}_2$  scale by the oxidation of the  $\text{SiC}$  phase, which shows parabolic oxidation behavior in the investigated temperature range.<sup>[17,18]</sup> It is well known, that the oxidation resistance of many polymer-derived ceramics relies on the formation of a  $\text{SiO}_2$  scale.<sup>[19–21]</sup>

The  $\text{SiC}$  phase oxidizes on the sample surface and along the interface between former powder particles and pure  $\text{SiC}$  regions (sinter necks), where the oxidized  $(\text{Hf}_x\text{Ta}_{1-x})\text{C}$  precipitates are also located. The element maps measured by EPMA and EDS (see Figure 5, 6, S1, S3, and S4, Supporting Information) as well as the TEM investigations (see Figure 8) of the oxidized  $(\text{Hf}_x\text{Ta}_{1-x})\text{C}/\text{SiC}$  samples show larger areas just below the sample surface, which are not completely oxidized. These are primarily the  $\text{SiC}$  sinter necks containing less  $(\text{Hf}_x\text{Ta}_{1-x})\text{C}$  precipitates, which are formed during the FAST sintering process.<sup>[11]</sup> Nevertheless, even within larger former powder particles, unoxidized  $(\text{Hf}_x\text{Ta}_{1-x})\text{C}$  precipitates are still present (see Figure 8). This illustrates the slowing effect of the  $\text{SiO}_2$  formation on the oxidation progress and the resulting plateau formation. However, regarding the plateau formation, it should also be noted that  $\text{CO}$  and  $\text{CO}_2$  can still be released by the oxidation of carbon within the different phases of the bulk during exposure, lowering the observed mass change. The isothermal section of the measurement is therefore also a kind of parabolic oxidation behavior, which consists of a superposition of an increase in mass due to oxide formation and a decrease in mass due to the release of  $\text{CO}$  and  $\text{CO}_2$ .

The comparison of the TGA curves (see Figure 1) and the mean specific mass gain (see Table 1) of the chemically modified samples reveals that  $(\text{Hf}_{0.7}\text{Ta}_{0.3})\text{C}/\text{SiC}$  experiences the lowest mass gain at both temperatures. This is related to the Hf/Ta ratio and the resulting phase composition. Comparison of the XRD patterns of the oxidized  $(\text{Hf}_x\text{Ta}_{1-x})\text{C}/\text{SiC}$  samples

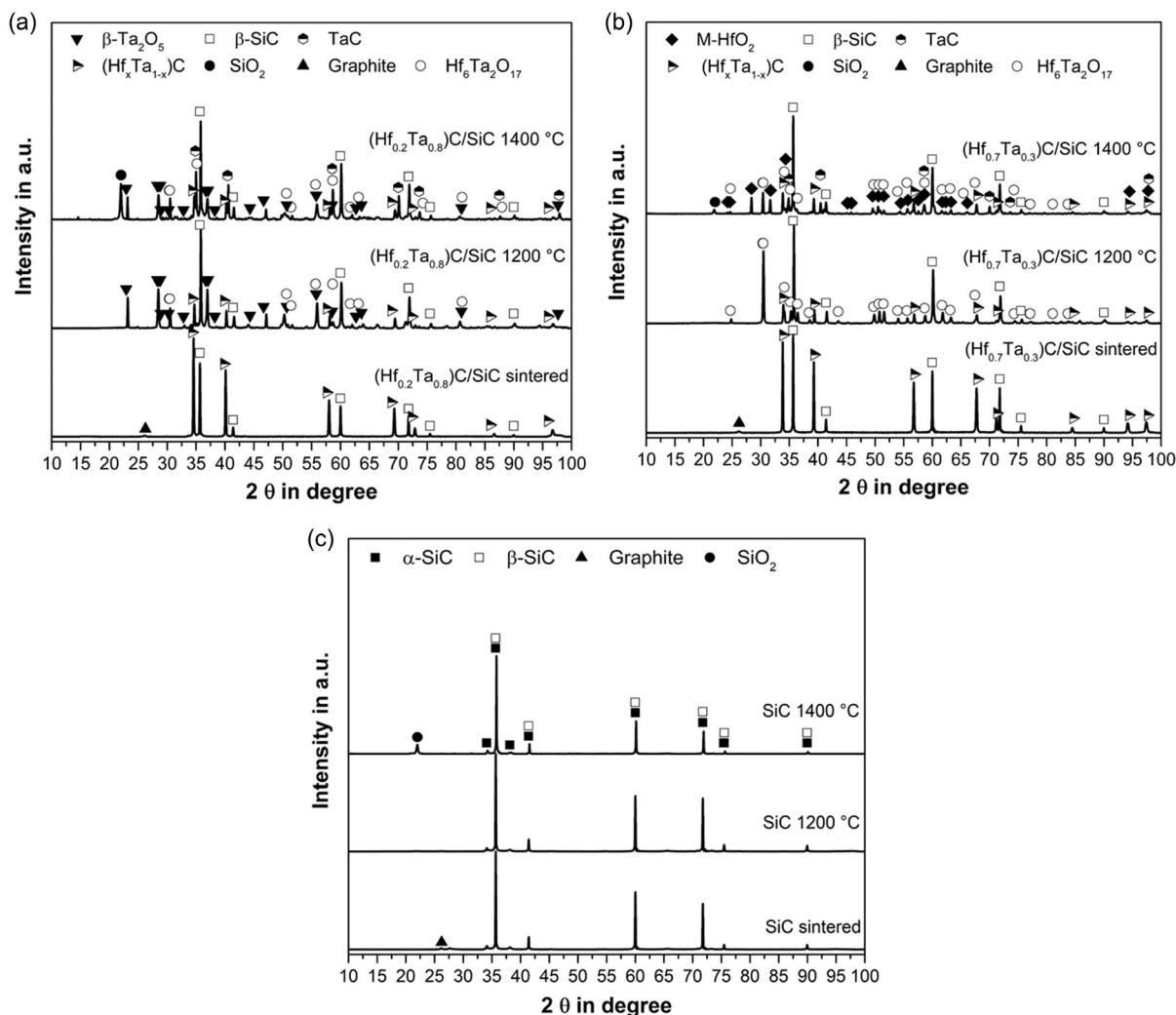


**Figure 9.** Diffraction patterns of  $(\text{Hf}_{0.2}\text{Ta}_{0.8})\text{C}/\text{SiC}$  (a),  $(\text{Hf}_{0.7}\text{Ta}_{0.3})\text{C}/\text{SiC}$  (b), and SiC (c) polymer-derived monoliths surface after field-assisted sintering and exposure for 50 h in synthetic air at 1200 and 1400 °C, respectively.

(see Figure 9a,b) shows that  $(\text{Hf}_{0.2}\text{Ta}_{0.8})\text{C}/\text{SiC}$  primarily forms  $\text{Ta}_2\text{O}_5$  and  $\text{Hf}_6\text{Ta}_2\text{O}_{17}$ , while  $(\text{Hf}_{0.7}\text{Ta}_{0.3})\text{C}/\text{SiC}$  forms  $\text{HfO}_2$  and  $\text{Hf}_6\text{Ta}_2\text{O}_{17}$ . These significant differences in the resulting phase composition can be explained with the help of the  $\text{HfO}_2\text{-Ta}_2\text{O}_5$  phase diagram published in 2019 by McCormack et al.<sup>[22]</sup> (see Figure 10). The reduction of the Hf/Ta ratio from  $(\text{Hf}_{0.7}\text{Ta}_{0.3})\text{C}/\text{SiC}$  to  $(\text{Hf}_{0.2}\text{Ta}_{0.8})\text{C}/\text{SiC}$  leads to the formation of  $\text{Ta}_2\text{O}_5$  besides  $\text{Hf}_6\text{Ta}_2\text{O}_{17}$ , which is verified by the XRD measurements. The diffractograms of  $(\text{Hf}_{0.2}\text{Ta}_{0.8})\text{C}/\text{SiC}$  show the formation of  $\text{Ta}_2\text{O}_5$  at both temperatures, while  $(\text{Hf}_{0.7}\text{Ta}_{0.3})\text{C}/\text{SiC}$  forms only  $\text{Hf}_6\text{Ta}_2\text{O}_{17}$  at 1200 °C (see Figure 9a,b).

Several authors observed a positive influence of the formation of  $\text{Hf}_6\text{Ta}_2\text{O}_{17}$  on the oxidation resistance.<sup>[6,8,14,23–30]</sup> For example, Yang et al.<sup>[24]</sup> investigated the oxidation resistance of Hf-Ta-alloys with varying Hf/Ta ratios, which were oxidized for 10 min at 1500 °C in laboratory air. They found an enhanced oxidation resistance of the Hf-26.7 at% Ta alloy, which formed a compact pure  $\text{Hf}_6\text{Ta}_2\text{O}_{17}$  oxide scale. Alloys with excess Hf (Ta) developed an oxide scale consisting of  $\text{Hf}_6\text{Ta}_2\text{O}_{17}$  and  $\text{HfO}_2$  ( $\text{Ta}_2\text{O}_5$ ).<sup>[24]</sup>

$\text{Hf}_6\text{Ta}_2\text{O}_{17}$  offers several advantages. First, it experiences no phase transition up to around 2244 °C<sup>[22]</sup> (see Figure 10) and, therefore, exhibits no detrimental change in volume in contrast to  $\text{Ta}_2\text{O}_5$ , which will be discussed in Section 4.3. In addition,  $\text{Hf}_6\text{Ta}_2\text{O}_{17}$  has a low thermal conductivity ( $1.62 \text{ W m}^{-1}\cdot\text{K}$  at 1500 °C<sup>[31]</sup>– $2.89 \text{ W m}^{-1}\cdot\text{K}$  at 1200 °C<sup>[32]</sup>) and it seems to have a low oxygen diffusivity.<sup>[6,8,24,25]</sup> Besides the positive influence on the oxidation behavior,  $\text{Hf}_6\text{Ta}_2\text{O}_{17}$  shows a high resistance against calcium-magnesium-alumina-silicate corrosion<sup>[33–36]</sup> and promising mechanical properties.<sup>[36,37]</sup> Overall,  $\text{Hf}_6\text{Ta}_2\text{O}_{17}$  seems to be a highly interesting candidate for future thermal barrier and environmental barrier coatings.<sup>[30,31,35,37–44]</sup>

The increased phase fraction of  $\text{Ta}_2\text{O}_5$  in  $(\text{Hf}_{0.2}\text{Ta}_{0.8})\text{C}/\text{SiC}$  influences the oxidation behavior in two ways. Besides the mass increase due to  $\text{Ta}_2\text{O}_5$  formation compared to the formation of  $\text{HfO}_2$  or  $\text{SiO}_2$  (see Section 4.1), the observed increased crack formation in  $(\text{Hf}_{0.2}\text{Ta}_{0.8})\text{C}/\text{SiC}$  (see Figure 3) is also due to this phase, which is explained in more detail in the following Section 4.3. The formed cracks facilitate the inward diffusion

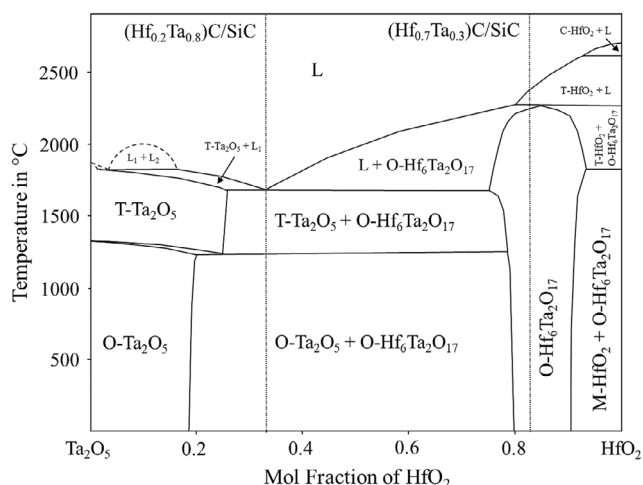


**Figure 10.** Schematic representation of the  $\text{HfO}_2\text{-Ta}_2\text{O}_5$  temperature phase diagram redrawn after McCormack et al.<sup>[22]</sup>

of oxygen and thus explain the increased mass gain and enhanced internal oxidation of  $(\text{Hf}_{0.2}\text{Ta}_{0.8})\text{C}/\text{SiC}$ , particularly at 1200 °C.

The assessment of the TGA curves reveals relatively high deviations of the measured specific mass gains (e.g.,  $(\text{Hf}_{0.7}\text{Ta}_{0.3})\text{C}/\text{SiC}$  at 1200 °C). This behavior is also due to the observed cracking, especially in the case of  $(\text{Hf}_{0.2}\text{Ta}_{0.8})\text{C}$ . Another explanation is the small sample size in this work, which results in a relatively larger influence of the sample edges on the oxidation behavior.<sup>[45,46]</sup>

### 3.3. Crack Formation

First, the oxidation from TaC to  $\text{Ta}_2\text{O}_5$  leads to a volume expansion, which can initialize cracking. Calculation of the Pilling–Bedworth ratio (PBR), which relates the molar volume of a metal oxide to the molar volume of the corresponding phase from which the oxide originates, already gives a clear impression of the volume expansion of the different phases of the investigated materials. The PBR of the oxidation of TaC to  $\text{Ta}_2\text{O}_5$  is 2.00 (oxidation of Ta to  $\text{Ta}_2\text{O}_5 = 2.47$ ) and therefore significantly higher than the PBR for the oxidation of HfC to  $\text{HfO}_2$  with 1.39 (oxidation of Hf to  $\text{HfO}_2 = 1.62$ ). An increased amount of  $\text{Ta}_2\text{O}_5$  therefore leads to crack initiation through volume expansion. Furthermore, the volume expansion of the  $(\text{Hf}_x\text{Ta}_{1-x})\text{C}$  precipitates during oxidation provides an explanation for the measured reduced porosity of the chemically modified samples after oxidation. It can be concluded that increased  $\text{Ta}_2\text{O}_5$  formation leads to crack initiation due to volume expansion during oxidation. The formed cracks thereby represent pathways for facilitated inward diffusion of oxygen, which is also an explanation for the increased internal oxidation of  $(\text{Hf}_{0.2}\text{Ta}_{0.8})\text{C}/\text{SiC}$  at 1200 °C.

Second, despite the volume expansion during oxidation,  $\text{Ta}_2\text{O}_5$  experiences an additional change in volume at  $\approx 1360$  °C through a phase transformation from orthorhombic  $\beta\text{-Ta}_2\text{O}_5$  to tetragonal  $\alpha\text{-Ta}_2\text{O}_5$ , which is accompanied by a decrease in volume of  $-2.32\%$ .<sup>[22]</sup> This phase transformation represents an

additional crack initiation mechanism during cooling of the samples investigated at 1400 °C. Furthermore, the calculated change in molar volume of  $\text{O-Ta}_2\text{O}_5$  and  $\text{O-Hf}_6\text{Ta}_2\text{O}_{17}$  of  $-25.24\%$  is large compared to  $\text{O-Hf}_6\text{Ta}_2\text{O}_{17}$  and  $\text{M-HfO}_2$  (3.07%).<sup>[22]</sup>

Besides the change in volume of  $\text{Ta}_2\text{O}_5$ , the coefficients of thermal expansion (CTE) as a third reason also can play a crucial role in the cracking behavior. In a study published in 2023, Nisar et al.<sup>[23]</sup> produced densified samples of  $\text{HfO}_2$  and  $\text{Ta}_2\text{O}_5$  powder using field-assisted sintering. After exposing the samples to a plasma arc-jet for up to 3 min, cracks were detected in 50 vol%  $\text{HfO}_2\text{-50 vol% Ta}_2\text{O}_5$  and 70 vol%  $\text{HfO}_2\text{-30 vol% Ta}_2\text{O}_5$  samples, which they attributed to the thermal expansion behavior of  $\text{Ta}_2\text{O}_5$ .<sup>[23]</sup> The CTE mismatch between the formed oxides  $\text{Ta}_2\text{O}_5$  ( $3 \times 10^{-6}\text{-}4 \times 10^{-6} \text{ K}^{-1}$ <sup>[47-49]</sup>) and  $\text{Hf}_6\text{Ta}_2\text{O}_{17}$  ( $9.06 \times 10^{-6} \text{ K}^{-1}$  at 1500 °C<sup>[31]</sup>) induces interfacial compressive stresses at the interface of both oxides, leading to an increased crack formation.<sup>[23]</sup> For the investigated  $(\text{Hf}_x\text{Ta}_{1-x})\text{C}/\text{SiC}$  nanocomposites the CTE mismatch of  $\text{Ta}_2\text{O}_5$  with SiC ( $5.1 \times 10^{-6} \text{ K}^{-1}$ <sup>[50,51]</sup>) and  $\text{SiO}_2$  ( $0.5 \times 10^{-6}\text{-}4.1 \times 10^{-6} \text{ K}^{-1}$ <sup>[52,53]</sup>) is smaller compared to the mismatch of  $\text{Hf}_6\text{Ta}_2\text{O}_{17}$  and the two phases, which indicates a lower cracking tendency at the interfaces of  $\text{Ta}_2\text{O}_5$  and SiC or  $\text{SiO}_2$  and a higher cracking tendency at the interface between  $\text{Hf}_6\text{Ta}_2\text{O}_{17}$  and SiC or  $\text{SiO}_2$ . The thermal expansion behavior is essential for cyclic tests and rapid cooling. However, no abnormalities were found during cooling in the tests carried out in this work. For future investigations, the cyclic oxidation behavior of the materials is of high interest for possible applications in a high temperature environment.

The negative influence of  $\text{Ta}_2\text{O}_5$  can also be seen in the investigation of other systems with the composition  $\text{A}_6\text{B}_2\text{O}_{17}$ .<sup>[54,55]</sup> A study by Liu et al.<sup>[38]</sup> on  $\text{Zr}_6\text{Ta}_2\text{O}_{17}$  thermal barrier coatings with different  $\text{Ta}_2\text{O}_5$  contents also confirmed the negative influence of  $\text{Ta}_2\text{O}_5$  on the high-temperature properties. They prepared  $\text{Zr}_6\text{Ta}_2\text{O}_{17}$  powders with different  $\text{Ta}_2\text{O}_5$  contents and subsequently applied them to a conventional thermal barrier coating system (Ni-based superalloys + NiCoCrAlY bond coat + YSZ thermal barrier coating) by atmospheric plasma spraying. The investigations showed an improvement in mechanical properties as well as in oxidation resistance in isothermal and cyclic tests of the  $\text{Zr}_6\text{Ta}_2\text{O}_{17}$  layer with decreasing  $\text{Ta}_2\text{O}_5$  content.<sup>[38]</sup>

### 3.4. Internal Oxidation of $(\text{Hf}_x\text{Ta}_{1-x})\text{C}/\text{SiC}$

The SEM and TEM images as well as the EPMA measurements (see Figure 5, 6, and 8) illustrate the microstructural evolution of the internal oxidation. The element maps show that oxygen is concentrated at the interface of the  $\beta\text{-SiC}$  and the former powder particles, where the nanosized  $(\text{Hf}_x\text{Ta}_{1-x})\text{C}$  are located (see Figure 7 and S1, Supporting Information).<sup>[11,56]</sup> This demonstrates that the internal oxidation is mainly related to the oxidation of the  $(\text{Hf}_x\text{Ta}_{1-x})\text{C}$ , which can be rationalized by the thermodynamics and oxidation kinetics of HfC and TaC.

Figure 11 depicts the Ellingham diagram of the main phases of the investigated materials. It can be seen that  $\text{HfO}_2$  and  $\text{Ta}_2\text{O}_5$  are very stable oxides whose formation is thermodynamically favored, so the corresponding carbides can only exist at low oxygen partial pressure. The free energy of formation of  $\text{HfO}_2$  is lower compared to the one of  $\text{SiO}_2$ , which means that the



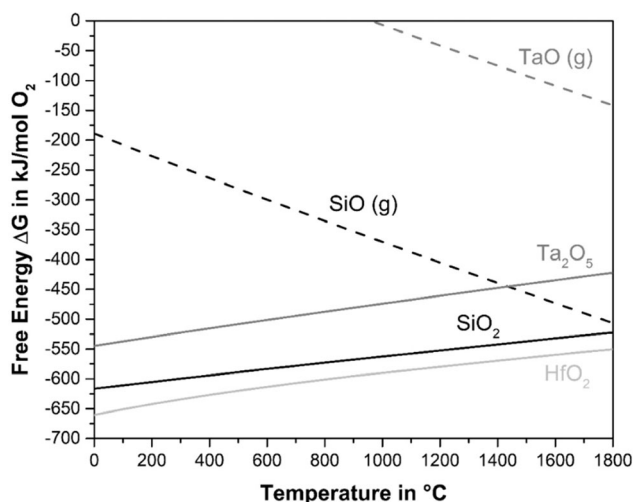


**Figure 11.** Ellingham diagram showing the free energy of formation over temperature of  $\text{HfO}_2$ ,  $\text{SiO}_2$ ,  $\text{Ta}_2\text{O}_5$ ,  $\text{SiO}$ , and  $\text{TaO}$  from the reaction with the corresponding carbides and oxygen.

reduction in oxygen partial pressure through the formation of a dense  $\text{SiO}_2$  is not capable to prevent the formation of  $\text{HfO}_2$ . Figure 11 shows that the free energy of formation of  $\text{SiO}_2$  is lower than that of  $\text{Ta}_2\text{O}_5$ , however, the formation of  $\text{Ta}_2\text{O}_5$  is detected in all oxidized samples of  $(\text{Hf}_{0.2}\text{Ta}_{0.8})\text{C}/\text{SiC}$ . Therefore, besides the thermodynamic perspective, kinetics additionally plays a central role as will be discussed below. The slow kinetics in forming a protective silica scale at 1200 °C is reported in literature,<sup>[4,6,8,18]</sup> the kinetics of  $\text{HfO}_2$  and  $\text{Ta}_2\text{O}_5$  formation are faster<sup>[4]</sup> and start in the temperature range of around 400 °C to 800 °C.<sup>[14–16]</sup> In this work, the STA measurements shown in Figure 2 indicate an onset temperature at around 600 °C (see Section 4.1). The faster oxidation kinetics explains the preferential oxidation of  $(\text{Hf}_x\text{Ta}_{1-x})\text{C}$  in addition to the performed thermodynamic calculations.

The comparison of the degree of internal oxidation at 1200 °C and 1400 °C reveals significant differences (see Figure 5). At 1200 °C, all three materials experience a high degree of internal oxidation, whereas at 1400 °C, the modified PDC-NCs  $(\text{Hf}_x\text{Ta}_{1-x})\text{C}/\text{SiC}$  develop an internal oxidation layer. The formation of the internal oxidation layer of the two materials could be related to three factors.

First, the diffraction patterns reveal cristobalite formation (see Figure 9a,b) at 1400 °C, which indicates the accelerated kinetics of silica formation through the increased temperature. Due to the higher exposure temperature of 1400 °C, the rate of  $\text{SiO}_2$  formation is accelerated,<sup>[18]</sup> and an outer oxide layer forms faster. In contrast, at 1200 °C it takes longer for  $\text{SiO}_2$  to form, which is associated with increased inward diffusion of oxygen during preheating and the first few hours of isothermal exposure, resulting in increased internal oxidation. This is supported by the measured TGA curves (see Figure 1), where a faster plateau formation can be observed at 1400 °C. Furthermore, studies by Wen et al.<sup>[8]</sup> show that the extent of internal oxidation can be reduced by the passivation of the samples at 1400 °C for 30 min in air, which leads to a faster formation of a protective  $\text{SiO}_2$  scale and underlines its influence on the internal oxidation.

Second, the thickness of the external oxide layer increases compared to 1200 °C by 80% from  $\approx 0.5$  to  $\approx 0.9$   $\mu\text{m}$  with increasing the temperature to 1400 °C. The thicker oxide scale seems to effectively hinder the inward diffusion of oxygen, which reduces the oxygen partial pressure in the bulk phase to a level where the oxidation of the  $(\text{Hf}_x\text{Ta}_{1-x})\text{C}$  can be limited. However, the layer thickness is not sufficient to completely prevent the internal oxidation of the samples. Layer thicknesses determined in the literature after an exposure of pure (CVD-)SiC for 50 h in air or  $\text{O}_2$  are in the range of  $0.95^{[17,18]}$ – $1.18$   $\mu\text{m}^{[17]}$  (1200 °C) and  $1.38$ – $2.40$   $\mu\text{m}^{[17,18]}$  (1400 °C). The comparison of the literature values with the layer thicknesses measured in this work shows that the oxide layers of the polymer-derived samples are thinner. The formed oxide scale thus has a lower barrier effect against the inward diffusion of oxygen, which also explains the observed internal oxidation of the SiC phase (see Figure 6, S3 and S4, Supporting Information) in the  $(\text{Hf}_x\text{Ta}_{1-x})\text{C}/\text{SiC}$  samples (see Section 4.2). However, the formation of  $\text{Hf}_6\text{Ta}_2\text{O}_{17}$  has a positive influence on the barrier effect of the oxide layer as discussed in Section 4.2.

Third, with increasing the temperature the viscosity of  $\text{SiO}_2$  increases,<sup>[4,57]</sup> which can induce self-healing of flaws, which may be an additional factor of the improved oxidation behavior, especially of  $(\text{Hf}_{0.2}\text{Ta}_{0.8})\text{C}/\text{SiC}$  at the higher temperature of 1400 °C.

Overall, the formed outer and inner oxide layer seems to be effective in slowing down the progress of oxidation, which is shown in the plateau formation with minimal mass changes and in the comparison of the layer thickness of the inner oxide layer at 1400 °C as a function of the exposure time. The internal oxidation scale thickness increases only by 29% ( $(\text{Hf}_{0.2}\text{Ta}_{0.8})\text{C}/\text{SiC}$ ) and 18% ( $(\text{Hf}_{0.7}\text{Ta}_{0.3})\text{C}/\text{SiC}$ ) even though the exposure time doubled from 50 to 100 h at 1400 °C. For the external oxide scale an increase from  $\approx 0.9$   $\mu\text{m}$  after 50 h to  $\approx 0.9$ – $1.2$   $\mu\text{m}$  after 100 h at 1400 °C could be observed.

### 3.5. TaC Formation

The diffraction patterns reveal other significant differences in the microstructure of the materials besides the  $\text{SiO}_2$  formation. Both  $(\text{Hf}_x\text{Ta}_{1-x})\text{C}/\text{SiC}$  materials show TaC formation at 1400 °C (see Figure 9a,b), which could not be detected at 1200 °C. The amount of TaC seems to increase from  $(\text{Hf}_{0.7}\text{Ta}_{0.3})\text{C}/\text{SiC}$  to  $(\text{Hf}_{0.2}\text{Ta}_{0.8})\text{C}/\text{SiC}$ , indicated by the intensity of the characteristic peaks. This effect is known from the literature.<sup>[6,8]</sup>

In addition to the TaC formation,  $(\text{Hf}_{0.7}\text{Ta}_{0.3})\text{C}/\text{SiC}$  experiences the development of monoclinic  $\text{HfO}_2$  at 1400 °C, which was not detected at 1200 °C. This effect was also measured by Wen et al.<sup>[6,8]</sup> who suggest a reduction of excess  $\text{Ta}_2\text{O}_5$  with Ta-depleted  $(\text{Hf}_x\text{Ta}_{1-x})\text{C}$  to form  $\text{HfO}_2$ . They stated that the Ta-depleted  $(\text{Hf}_x\text{Ta}_{1-x})\text{C}$  form due to faster oxidation kinetics of Ta in comparison to Hf. However, the explanation seems rather implausible under the experimental parameters used. The thermodynamic calculations in Section 4.4 show that the oxidation of Hf is thermodynamically favored to that of Ta (see Figure 11). Furthermore, the exposure time of 50 h and 100 h, respectively, is rather long and the isothermal temperature of 1200 and 1400 °C, respectively, is relatively high, which is why

kinetic aspects of the oxidation reaction of Ta and Hf play a minor role for the phase composition of the samples after exposure.

A possible explanation could be the preferential oxidation of Hf, which would lead to Hf-depleted ( $\text{Hf}_x\text{Ta}_{1-x}$ )C and therefore to a shift towards carbides with an increased Ta content. This would also explain the increased peak intensity of TaC in the material with a lower Hf/Ta ratio ( $\text{Hf}_{0.2}\text{Ta}_{0.8}$ )C/SiC.

The results of recent investigations by Backman et al.<sup>[58,59]</sup> support this explanation. The authors investigated the oxidation behavior of high entropy UHTCs dogbone specimens, which were oxidized in 1 vol%  $\text{O}_2$  at 1700 °C for 5 min using a resistive heating system via Joule heating. The chosen materials were high entropy carbides and diborides consisting of group IV and V elements. Backman et al. found a preferential oxidation of the thermodynamically more stable group V elements Hf, Zr, and Ti, leading to an enrichment of the substrate with group V elements Nb and Ta. The order of oxidation of the elements correlates with the thermodynamic favorability of the corresponding oxides.<sup>[59]</sup>

Also Yang et al.<sup>[24]</sup> who investigated the oxidation behavior of Hf-Ta alloys for 10 min of exposure at 1500 °C in laboratory air, stated that the incorporation of oxygen led to precipitation of  $\alpha$ -HfO leaving behind a Ta-enriched HfTa solid solution. The  $\alpha$ -HfO oxidizes further to monoclinic  $\text{HfO}_2$  with increasing oxygen addition.<sup>[24]</sup>

The preferential oxidation of Hf also provides an explanation for another significant difference arising when comparing the diffraction patterns of ( $\text{Hf}_{0.7}\text{Ta}_{0.3}$ )C/SiC (see Figure 9b). It can be seen that with increasing temperature from 1200 to 1400 °C ( $\text{Hf}_{0.7}\text{Ta}_{0.3}$ )C/SiC develops  $\text{HfO}_2$  as an additional oxide to  $\text{Hf}_6\text{Ta}_2\text{O}_{17}$  at 1200 °C, which was also observed by Wen et al.<sup>[6]</sup> This result is discussed in terms of the improved oxidation resistance at 1400 °C. The thicker oxide scale reduces the oxygen partial pressure in the bulk phase, which leads to the development of an internal oxide layer by limiting internal oxidation. The reduction of the oxygen partial pressure at 1400 °C seems to be high enough to prevent the oxidation of Ta, leading to selective oxidation of Hf to  $\text{HfO}_2$ , leaving behind Hf-depleted ( $\text{Hf}_x\text{Ta}_{1-x}$ )C, whereas at 1200 °C the reduction in oxygen partial pressure is not high enough. For ( $\text{Hf}_{0.2}\text{Ta}_{0.8}$ )C/SiC the free  $\text{HfO}_2$  seems to be consumed by the reaction with  $\text{Ta}_2\text{O}_5$  to form  $\text{Hf}_6\text{Ta}_2\text{O}_{17}$ , explaining the missing  $\text{HfO}_2$  signal of this material.

## 4. Conclusion

The oxidation behavior of ( $\text{Hf}_x\text{Ta}_{1-x}$ )C/SiC nanocomposites bulk samples was investigated at 1200 and 1400 °C for up to 100 h in dry synthetic air. The results shed light on several interesting aspects: 1) The chemical modification of the polycarbosilane-based precursor with Hf and Ta leads to a significant reduction of the initial mass loss of the samples due to the oxidation of a free carbon phase. This finding attributed to i) a simultaneous mass increase due to the oxidation of the ( $\text{Hf}_x\text{Ta}_{1-x}$ )C precipitates superimposing the mass loss due to CO and  $\text{CO}_2$  formation, which also shifts the onset temperature of mass loss to higher temperatures, ii), reduction of the porosity of the samples due to the chemical modification of the precursor, which has a

positive effect on the oxidation resistance and thus also reduces the oxidation of the free carbon phase and formation of volatile CO and  $\text{CO}_2$ . Thus, an improved densification of the modified materials under the used process parameters was observed. 2) The oxidation mechanism of the ( $\text{Hf}_x\text{Ta}_{1-x}$ )C/SiC nanocomposites is governed by two effects. First, the preferential oxidation of ( $\text{Hf}_x\text{Ta}_{1-x}$ )C, which is explained by the different thermodynamic stability of the corresponding oxides  $\text{HfO}_2$ ,  $\text{Ta}_2\text{O}_5$ , and  $\text{Hf}_6\text{Ta}_2\text{O}_{17}$ . Consequently, low oxygen partial pressures are sufficient for the oxidation of the carbide precipitates. Second, the oxidation kinetics of  $\text{SiO}_2$  at the investigated temperatures of 1200 and 1400 °C: At 1200 °C, the  $\text{SiO}_2$  formation is not fast enough to significantly reduce the inward diffusion of oxygen into the bulk phase during the first hours of exposure, which explains the high degree of internal oxidation at this temperature. In contrast, at 1400 °C the faster  $\text{SiO}_2$  formation leads to reduced internal oxidation. 3) Shifting the Hf/Ta ratio from ( $\text{Hf}_{0.2}\text{Ta}_{0.8}$ )C/SiC to ( $\text{Hf}_{0.7}\text{Ta}_{0.3}$ )C/SiC results in an improved oxidation behavior at both temperatures. As reasons for this finding, an increased formation of  $\text{Hf}_6\text{Ta}_2\text{O}_{17}$  going along with a reduction of  $\text{Ta}_2\text{O}_5$  formation is identified.  $\text{Ta}_2\text{O}_5$  induces stress due to a large volume increase during oxidation. This phenomenon explains the increased crack formation and higher mass gain, especially at 1200 °C of ( $\text{Hf}_{0.2}\text{Ta}_{0.8}$ )C/SiC.  $\text{Hf}_6\text{Ta}_2\text{O}_{17}$  shows no phase transition up to temperatures >2000 °C. It is partially integrated into the Si-based oxide scale, which further reduces the oxygen permeability of the oxide scale and thereby increase the oxidation resistance.

Overall, the chemical modification of Si-based preceramic polymers with transition metals forming UHTC phases is a promising way to develop ceramic compositions with advanced oxidation resistance for applications in corrosive and high-temperature environments such as EBCs, TBCs, or CMCs (ceramic matrix composites).

## 5. Experimental Section

**Sample Preparation:** Two  $\text{Si}(\text{Hf}_x\text{Ta}_{1-x})\text{C}$  single-source precursors were synthesized with different Hf/Ta ratios (i.e.,  $x = 0.2$  and  $x = 0.7$ ) by reacting the commercially available polycarbosilane (SMP-10, Starfire System Inc, Glenville, USA) with tetrakis(diethylamido)hafnium(IV) (TDEAH, 99.99%, Sigma-Aldrich Chemie GmbH, Taufkirchen, Germany) and pentakis(dimethylamido)tantalum(V) (PDMTA, 99.99%, Sigma-Aldrich Chemie GmbH, Taufkirchen, Germany) under purified Ar using the standard Schlenk technique. The ratio of metal complexes (TDEAH + PDMAT) to SMP-10 was set to 3:7. The molar ratio Hf:Ta was set accordingly to 2:8 and 7:3 for the production of  $\text{Si}(\text{Hf}_{0.2}\text{Ta}_{0.8})\text{C}$  and  $\text{Si}(\text{Hf}_{0.7}\text{Ta}_{0.3})\text{C}$ .

For the pyrolysis of the single-source precursors the samples were heated up to 1000 °C in Ar with two holding steps at 250 °C for 3 h and 1000 °C for 2 h using a quartz Schlenk tube and crucible. Subsequently, the resulting amorphous powders were milled using an agate pestle and mortar and sieved to a grain size of  $\geq 100 \mu\text{m}$ .

The amorphous  $\text{Si}(\text{Hf}_x\text{Ta}_{1-x})\text{C}$  powders were densified to ( $\text{Hf}_x\text{Ta}_{1-x}$ )C/SiC ceramic bulk nanocomposites using FAST (FCT HP D 25/1, FCT Systeme GmbH, Frankenblick, Germany). The samples were heated up with 100 °C  $\text{min}^{-1}$  to the target temperature of 2200 °C with a subsequent holding time of 20 min under uniaxial pressure of 50 MPa. They were cooled down to room temperature with a cooling rate of 220 °C  $\text{min}^{-1}$ . Detailed information on the synthesis and densification of the single-source precursors can be found in refs. [6,11,60–62].

To prepare the samples for TGA the ceramic bulk disks were cut into pieces with surface sizes ranging from 0.4 to 1.2 cm<sup>2</sup> using a cut-off machine (Accutom-50, Struers, Copenhagen, Denmark) equipped with a diamond cut-off wheel (B152, ATM Qness GmbH, Mammelzen, Germany). Subsequently, the ceramic monoliths were ground with SiC-paper (Struers, Copenhagen, Denmark) with a final grain size of 22 μm (P800 grit/ANSI #400) and afterwards cleaned for 10 min in acetone using an ultrasonic bath. To measure the surface areas of the sintered monoliths images with a stereo microscope (MZ16 A, Leica Microsystems GmbH, Wetzlar, Germany) equipped with a camera DMC 2900 (Leica Microsystems GmbH, Wetzlar, Germany) were taken and evaluated by using an image processing program<sup>[12]</sup> (Image), National Institutes of Health, USA).

**Thermogravimetric Analysis:** Thermogravimetric analysis was used to assess the oxidation kinetics. A vertical furnace (RHT04/17S, Nabertherm GmbH, Lilienthal, Germany) equipped with an analytical balance (B24, SETARAM Instrumentation, Caluire, France) was used. The samples were placed in an Al<sub>2</sub>O<sub>3</sub>-crucible with air slots, connected with a Pt-wire to the pan in a hang-down setup. The temperature program involved preheating with 15 °C min<sup>-1</sup> up to 1000 °C and 5 °C min<sup>-1</sup> until the isothermal temperature was reached. The dwell times were 50 and 100 h at 1200 and 1400 °C, respectively. After the dwell time, the samples were cooled down to room temperature by switching off the heating for the samples oxidized at 1200 °C. To improve the comparability of the cooling segment, the samples oxidized at 1400 °C were cooled down to 1200 with 15 °C min<sup>-1</sup> followed by switching off the heating. Preheating, isothermal heating as well as cooling were carried out under constant gas flow of synthetic air (79.5 vol% N<sub>2</sub>/20.5 vol% O<sub>2</sub>, ALPHAGAZ 1, L'Air Liquide S.A., Paris, France) of 4.5 L h<sup>-1</sup> (gas velocity of 10.6 cm min<sup>-1</sup>).

To further elucidate the oxidation behavior during the preheating step, one sample of each material was investigated using STA combining thermogravimetry with differential scanning calorimetry (STA 449 F3 Jupiter, NETZSCH-Gerätebau GmbH, Selb, Germany). The samples were placed in an Al<sub>2</sub>O<sub>3</sub>-crucible with a lid (Ø 6.8 mm, 85 μL, NETZSCH-Gerätebau GmbH, Selb, Germany). The samples were heated up to 1200 °C with 15 °C min<sup>-1</sup> in a synthetic air gas flow of 50 mL min<sup>-1</sup> (79.5 vol% N<sub>2</sub>/20.5 vol% O<sub>2</sub>, ALPHAGAZ 1, Air Liquide S.A., Paris, France). After a dwell time of 5 h the samples were cooled down with 15 °C min<sup>-1</sup> to room temperature. As a baseline measurement empty Al<sub>2</sub>O<sub>3</sub>-crucibles with lids were used.

**Characterization Methods:** The phase composition of the sintered and oxidized samples was investigated by XRD (D8 Advance, Bruker AXS, Karlsruhe, Germany). The patterns were recorded by using Ni-filtered Cu-Kα radiation, a step size of 0.02° with 1 s per step in the measurement range from 10° to 100°. For the analysis of the patterns the Match! Software (Crystal Impact - Dr. H. Putz & Dr. K. Brandenburg GbR, Bonn, Germany) was used to perform a baseline correction and index diffraction peaks with the PDF-2 database.<sup>[63]</sup>

For microstructural investigations, cross sections of the oxidized bulk ceramic were cut using a low-speed ISOMET diamond saw (Buehler, ITW Test & Measurement GmbH, Leinfelden-Echterdingen, Germany) and polished via a MultiPrep™ tripod polishing system (Allied High Tech Products Inc., California, USA) using diamond lapping film disks with decreasing grit sizes of 15, 9, 6, 3 μm and a final polishing step with the 1 μm diamond lapping film.

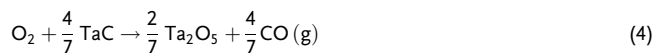
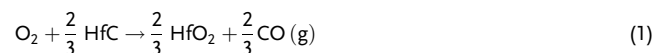
To assess the extent of oxidation attack of the samples, semiquantitative element maps of the cross-sectioned samples after oxidation were measured using EPMA (JXA-8100, JEOL Ltd., Akishima, Japan) equipped with five wavelength dispersive X-ray spectrometers (WDX). The size of the element maps was approximately half of the sample thickness for each measurement. For the measurements an acceleration voltage of 15 kV, a dwell time of 30 ms per pixel and a probe current of 30 nA was used. The following standards were used for obtaining the element maps: Fe<sub>4</sub>N (as standard for N), Cr<sub>3</sub>C<sub>2</sub> (as standard for C), Al<sub>2</sub>O<sub>3</sub> (as standard for O), and pure metallic Si, Hf, and Ta.

SEM analysis was performed on a JSM-7600 F instrument (JEOL Ltd, Tokyo, Japan) coupled with an X-Max EDS detector (Oxford Instruments, Abingdon, UK). BSE and SE images were taken at an acceleration voltage

of 15 kV and a working distance of 8 mm. The beam size diameter was smaller than 2 nm, and the acquisition time for each EDS point measurement was 30 s with an estimated relative error of ≈5%.

The microstructure and morphology of the oxidized ceramics were analyzed using transmission electron microscopy (TEM). TEM foil preparation followed a standard ceramographic preparation technique via grinding and polishing, as described above. The polished specimen (specimen thickness ≈ 15 μm) was then glued onto a TEM grid, followed by subsequent argon ion milling using the precision DuoMill 600DIF (Gatan Inc., California, USA) until perforation occurred. TEM analysis was conducted on a JEM-2100F microscope (JEOL Ltd. Tokyo, Japan) operating at an accelerating voltage of 200 kV, equipped with an X-Max EDS detector (Oxford Instruments, Abingdon, UK), a charge-coupled device camera and a JEOL beryllium double-tilt holder for sample orientation. TEM bright-field (TEM-BF), electron diffraction via the SAED technique, and EDS analyses were employed to gain microstructural, crystallographic, and chemical information. The as-prepared SEM and TEM samples were coated with carbon to avoid charging under the incident electron beam.

To assess the thermodynamic favorability of the detected phases the reaction module of FactSage<sup>[64]</sup> (Version 8.1) was used to calculate the Gibbs free energies per mol O<sub>2</sub>. The free energies of formation of the following five reactions were calculated for the temperature range from 0 to 1500 °C in steps of 100 °C:



## Supporting Information

Supporting Information is available from the Wiley Online Library or from the author.

## Acknowledgements

This study was conducted within the framework of the Research Training Group RTG 2561 "Materials Compounds from Composite Materials", which is funded by the DFG (German Research Foundation, Project no. 413956820). The authors thank Melanie Thalheimer and Dr. Gerald Schmidt from the Materials and Corrosion department of DECHEMA-Forschungsinstitut for the SEM images, EDS maps, and EPMA measurements. The authors thank Prof. Dr. Martin Bram from the IEK-1 of Forschungszentrum Jülich for spark plasma sintering of the samples. The authors thank Prof. Dr. Hans-Joachim Kleebe for his advice and suggestions in the field of electron microscopy.

Open Access funding enabled and organized by Projekt DEAL.

## Conflict of Interest

The authors declare no conflict of interest.

## Data Availability Statement

The data that support the findings of this study are available in the supplementary material of this article.



## Keywords

oxidation resistance, polymer-derived ceramic nanocomposites, TEM, thermogravimetry, ultra-high temperature ceramics

Received: November 29, 2023

Revised: February 14, 2024

Published online: February 23, 2024

- [1] E. Ionescu, S. Bernard, R. Lucas, P. Kroll, S. Ushakov, A. Navrotsky, R. Riedel, *Adv. Eng. Mater.* **2019**, *21*, 1900269.
- [2] W. G. Fahrenholtz, G. E. Hilmas, *Scr. Mater.* **2017**, *129*, 94.
- [3] W. G. Fahrenholtz, G. E. Hilmas, I. G. Talmy, J. A. Zaykoski, *J. Am. Ceram. Soc.* **2007**, *90*, 1347.
- [4] K. A. Kane, B. A. Pint, D. Mitchell, J. A. Haynes, *J. Eur. Ceram. Soc.* **2021**, *41*, 6130.
- [5] M. M. Opeka, I. G. Talmy, E. J. Wuchina, J. A. Zaykoski, S. J. Causey, *J. Eur. Ceram. Soc.* **1999**, *19*, 2405.
- [6] Q. Wen, R. Riedel, E. Ionescu, *Corros. Sci.* **2018**, *145*, 191.
- [7] M. M. Opeka, I. G. Talmy, J. A. Zaykoski, *J. Mater. Sci.* **2004**, *39*, 5887.
- [8] Q. Wen, R. Riedel, E. Ionescu, *Adv. Eng. Mater.* **2019**, *21*, 1800879.
- [9] Q. Wen, F. Qu, Z. Yu, M. Graczyk-Zajac, X. Xiong, R. Riedel, *J. Adv. Ceram.* **2022**, *11*, 197.
- [10] G. Barroso, Q. Li, R. K. Bordia, G. Motz, *J. Mater. Chem. A* **2019**, *7*, 1936.
- [11] N. Thor, G. Winkens, J. Bernauer, N.-C. Petry, K. Beck, J. Wang, R. Schwaiger, R. Riedel, H.-J. Kleebe, U. Kolb, M. Lepple, A. Pundt, *Adv. Eng. Mater.* **2023**.
- [12] C. A. Schneider, W. S. Rasband, K. W. Eliceiri, *Nat. Methods* **2012**, *9*, 671.
- [13] Q. Wen, Z. Yu, R. Riedel, *Prog. Mater. Sci.* **2020**, *109*, 100623.
- [14] C. Zhang, A. Loganathan, B. Boesl, A. Agarwal, *Coatings* **2017**, *7*, 111.
- [15] S. Shimada, *Solid State Ionics* **2002**, *149*, 319.
- [16] T. Glechner, O. E. Hudak, T. Wojcik, L. Haager, F. Bohrn, H. Hutter, O. Hunold, J. Ramm, S. Kolozsvári, E. Pitthan, D. Primetzhofer, H. Riedl, *Mater. Des.* **2021**, *211*, 110136.
- [17] J. Li, P. Eveno, A. M. Huntz, *Mater. Corros.* **1990**, *41*, 716.
- [18] L. U. J. T. Ogbuji, E. J. Opila, *J. Electrochem. Soc.* **1995**, *142*, 925.
- [19] E. J. Opila, N. S. Jacobson, in *Applications*, Vol. 4 (Eds: R. Riedel, I.-W. Chen), Wiley-VCH; John Wiley & Sons, Inc, Berlin, Hoboken, NJ **2013**, p. 3.
- [20] N. Jacobson, *Curr. Opin. Solid State Mater. Sci.* **2001**, *5*, 301.
- [21] K. G. Nickel, in *Precursor-Derived Ceramics* (Eds: J. Bill, F. Wakai, F. Aldinger), Wiley, Weinheim **1999**, p. 188.
- [22] S. J. McCormack, K.-P. Tseng, R. J. K. Weber, D. Kapush, S. V. Ushakov, A. Navrotsky, W. M. Kriven, *J. Am. Ceram. Soc.* **2019**, *102*, 4848.
- [23] A. Nisar, C. Zhang, B. Boesl, A. Agarwal, *Ceram. Int.* **2023**, *49*, 783.
- [24] Y. Yang, J. H. Perepezko, C. Zhang, *Mater. Chem. Phys.* **2017**, *197*, 154.
- [25] J. Zhang, S. Wang, W. Li, Y. Yu, J. Jiang, *Corros. Sci.* **2020**, *164*, 108348.
- [26] C. Zhang, *FIU Electronic Theses and Dissertations*, Miami **2016**, p. 2985, <https://digitalcommons.fiu.edu/etd/2985>.
- [27] C. Zhang, B. Boesl, A. Agarwal, *Ceram. Int.* **2017**, *43*, 14798.
- [28] A. Nisar, T. Sakthivel, C. Zhang, B. Boesl, S. Seal, A. Agarwal, *Appl. Surf. Sci.* **2022**, *592*, 153247.
- [29] A. Nisar, T. Dolmetsch, T. Paul, T. S. Sakthivel, C. Zhang, B. Boesl, S. Seal, A. Agarwal, *J. Am. Ceram. Soc.* **2022**, *105*, 2500.
- [30] M. Sanchez, K. A. Acord, S. Frueh, L. M. Rueschhoff, O. A. Graeve, *Adv. Eng. Mater.* **2023**, *25*, 2300138.
- [31] H. Li, Y. Yu, S. Wang, P. Xiao, T. Hu, *Ceram. Int.* **2021**, *47*, 17711.
- [32] M. Li, Q. Xu, L. Wang, *Key Eng. Mater.* **2010**, *434–435*, 459.
- [33] S. Liu, Q. Liu, X. Hu, J. Guo, W. Zhu, F. Zhang, J. Xia, *Coatings* **2023**, *13*, 404.
- [34] S. Liu, X. P. Hu, Q. Liu, J. W. Guo, J. Y. Wu, W. Zhu, *Corros. Sci.* **2022**, *208*, 110712.
- [35] H. Li, Y. Yu, B. Fang, P. Xiao, S. Wang, *J. Eur. Ceram. Soc.* **2022**, *42*, 4651.
- [36] Z. Y. Tan, Z. H. Yang, W. Zhu, L. Yang, Y. C. Zhou, X. P. Hu, *Ceram. Int.* **2020**, *46*, 25242.
- [37] Q. Wu, K. Cao, Y. Sun, C. Li, L. Yang, Y. C. Zhou, *Ceram. Int.* **2022**, *48*, 31461.
- [38] Q. Liu, X. Hu, W. Zhu, J. Guo, Z. Tan, *J. Am. Ceram. Soc.* **2021**, *104*, 6533.
- [39] M. Li, Q. Xu, L. Wang, *Key Eng. Mater.* **2012**, *512–515*, 635.
- [40] S. J. McCormack, R. J. Weber, W. M. Kriven, *Acta Mater.* **2018**, *161*, 127.
- [41] H. Li, Y. Yu, B. Fang, P. Xiao, S. Wang, *Ceram. Int.* **2022**, *48*, 13516.
- [42] A. A. Voskanyan, K. Lilova, S. J. McCormack, W. M. Kriven, A. Navrotsky, *Scr. Mater.* **2021**, *204*, 114139.
- [43] Q. Yang, H. Charalambous, E. M. Sobalvarro, J. Rivera, P. W. F. Evans, J. T. Cahill, W. L. Du Frane, J. D. Kuntz, *J. Eur. Ceram. Soc.* **2023**, *43*, 4541.
- [44] R. Jackson Spurling, C. Skidmore, N. S. McIlwaine, J.-P. Maria, *J. Mater. Sci.* **2023**, *58*, 6164.
- [45] N.-C. Petry, A. S. Ulrich, B. Feng, E. Ionescu, M. C. Galetz, M. Lepple, *J. Am. Ceram. Soc.* **2022**, *105*, 5380.
- [46] K. Shugart, B. Patterson, D. Lichtman, S. Liu, E. Opila, *J. Am. Ceram. Soc.* **2014**, *97*, 2279.
- [47] Y. S. Touloukian, R. K. Kirby, E. R. Taylor, T. Y. R. Lee, *Thermal Expansion: Nonmetallic Solids*, Plenum Publishing Corporation, New York, Washington **1977**.
- [48] M. Moldovan, C. M. Weyant, D. L. Johnson, K. T. Faber, *J. Therm. Spray Technol.* **2004**, *13*, 51.
- [49] Y. W. Bae, W. Y. Lee, D. P. Stinton, *J. Am. Ceram. Soc.* **1995**, *78*, 1297.
- [50] Z. Li, R. C. Bradt, *J. Mater. Sci.* **1986**, *21*, 4366.
- [51] K. N. Lee, R. A. Miller, N. S. Jacobson, *J. Am. Ceram. Soc.* **1995**, *78*, 705.
- [52] J.-H. Zhao, T. Ryan, P. S. Ho, A. J. McKerrow, W.-Y. Shih, *J. Appl. Phys.* **1999**, *85*, 6421.
- [53] H. Tada, A. E. Kumpel, R. E. Lathrop, J. B. Slanina, P. Nieve, P. Zavracky, I. N. Miaoulis, P. Y. Wong, *J. Appl. Phys.* **2000**, *87*, 4189.
- [54] S. J. McCormack, W. M. Kriven, *Acta Crystallogr., Sect. B* **2019**, *75*, 227.
- [55] M. Löffler, O. Fabricznaya, P. Hutterer, M. Lepple, *J. Eur. Ceram. Soc.* **2023**, *43*, 7668.
- [56] N. Thor, J. Bernauer, N.-C. Petry, E. Ionescu, R. Riedel, A. Pundt, H.-J. Kleebe, *J. Eur. Ceram. Soc.* **2022**, *43*, 1417.
- [57] G. Urbain, Y. Bottinga, P. Richet, *Geochim. Cosmochim. Acta* **1982**, *46*, 1061.
- [58] L. Backman, J. Gild, J. Luo, E. J. Opila, *Acta Mater.* **2020**, *197*, 20.
- [59] L. Backman, J. Gild, J. Luo, E. J. Opila, *Acta Mater.* **2020**, *197*, 81.
- [60] Q. Wen, Y. Xu, B. Xu, C. Fasel, O. Guillon, G. Buntkowsky, Z. Yu, R. Riedel, E. Ionescu, *Nanoscale* **2014**, *6*, 13678.
- [61] Q. Wen, Z. Yu, Y. Xu, Y. Lu, C. Fasel, K. Morita, O. Guillon, G. Buntkowsky, E. Ionescu, R. Riedel, *J. Mater. Chem. C* **2018**, *6*, 855.
- [62] Q. Wen, *Dissertation*, TU Darmstadt, TUpriprints, Darmstadt **2017**.
- [63] S. Gates-Rector, T. Blanton, *Powder Diffr.* **2019**, *34*, 352.
- [64] C. W. Bale, E. Béglise, P. Chartrand, S. A. Decterov, G. Eriksson, A. E. Gheribi, K. Hack, I.-H. Jung, Y.-B. Kang, J. Melançon, A. D. Pelton, S. Petersen, C. Robelin, J. Sangster, P. Spencer, M.-A. van Ende, *Calphad* **2016**, *54*, 35.